Evolution of Cloud Droplet Temperature and Lifetime in Spatiotemporally Varying Subsaturated Environments with Implications for Ice Nucleation at Cloud Edges

Puja Roy[1,2], Robert M. Rauber[1], Larry Di Girolamo[1]

[1]Department of Climate, Meteorology & Atmospheric Sciences, University of Illinois Urbana-Champaign, USA

[2]Research Applications Laboratory, NSF National Center for Atmospheric Research, USA

Correspondence to: Puja Roy (pujaroy@ucar.edu)

Abstract. Ice formation mechanisms in generating cells near stratiform cloud-tops, where mixing and entrainment occurs in the presence of supercooled water droplets, remain poorly understood. Supercooled cloud droplet temperature and lifetime may impact heterogeneous ice nucleation through contact and immersion freezing; however, modeling studies normally assume droplet temperature to be spatially uniform and equal to the ambient temperature. Here, we present a first-of-its-kind quantitative investigation of the temperature and lifetime of evaporating droplets, considering internal thermal gradients within the droplet as well as thermal and vapor density gradients in the surrounding air. Our approach employs solving the Navier-Stokes and continuity equations, coupled with heat and vapor transport, using an advanced numerical model. For typical ranges of cloud droplet sizes and environmental conditions, the droplet internal thermal gradients dissipate quickly ($\leq$ 0.3 s) when droplets are introduced to new subsaturated environments. However, the magnitude of droplet cooling is much greater than estimated from past studies of droplet evaporation, especially for drier environments. For example, for an environment with pressure of 500 hPa, and ambient temperature far from the droplet of -5°C, the droplet temperature reduction can be as high as 24, 11, and 5°C for initial ambient relative humidities of 10%, 40%, and 70% respectively. Droplet lifetimes are found to be tens of seconds longer compared to previous estimates due to weaker evaporation rates because of lower droplet surface temperatures. Using these new end-of-lifetime droplet temperatures, the enhancement in activation of ice-nucleating particles predicted by current ice nucleation parameterization schemes is discussed.

1 Introduction

Ice formation often occurs near cloud tops of stratiform clouds where ice-generating cells (AMS 2024) are frequently found in a variety of cold, cloudy environments (Plummer et al., 2014; Ramelli et al., 2021). These cells play a crucial role in primary ice nucleation and growth (Tessendorf et al., 2015). Evidence of mixing and entrainment and the presence of supercooled liquid water within and between the highly turbulent cells has been observed (Plummer et al., 2014; Wang et al., 2020; Zaremba et al., 2024). Within regions of entrainment and mixing at cloud boundaries, cloud droplets are exposed to subsaturated environments and undergo evaporation that leads to droplet temperatures that could be several degrees lower than that of the ambient environment (Kinzer and Gunn, 1951; Watts, 1971; Roy et al., 2023). However, in modeling cloud microphysical processes, the difference in temperature between the cloud droplets and their environment is generally assumed to be negligible (Pruppacher and Klett, 1997), i.e., the droplets' temperatures are approximated to be the same as that of their ambient environment. This assumption is reasonable for cloud droplets inside the cloud but breaks down within entrainment and mixing zones at cloud boundaries and may lead to uncertainties in the numerical simulations of microphysical processes. Cloud droplet temperatures affect the calculated droplet diffusional growth or evaporation rates (Roach 1976; Srivastava and Coen 1992; Marquis and Harrington 2005; Roy et al., 2023), and droplet lifetimes (Roy et al., 2023), radiative effects via temperature-dependent refractive indices (Rowe et al. 2020), and ice formation via pathways that require supercooled liquid water droplets, such as contact nucleation (Young, 1974), immersion freezing (Szakáll et al., 2021), and homogeneous nucleation (Khvorostyanov and Sassen, 1998; Khain and Pinsky, 2018). These uncertainties can propagate into microphysical parameterization schemes, leading to possible inadequate representation of mixed-phase cloud properties across various scales (e.g., Large Eddy Simulations (LES), Cloud Resolving Models (CRM), Climate Models), impacting predictions of precipitation or climate change.

Several studies have highlighted the special importance of the air-water interface of the water droplet during ice nucleation. Many experimental and theoretical studies have suggested that ice initiation occurs at the droplet surface (Tabazadeh et al., 2002a; Tabazadeh et al., 2002b; Djikaev et al., 2002; Satoh et al. 2002; Shaw et al., 2005) and the interface thermodynamically favors the contact mode over the immersion freezing mode (Djikaev and Ruckenstein, 2008). Based on their laboratory observations, Tabazadeh et al., (2002a) suggested that homogeneous nucleation of nitric acid dihydrate (NAD) and nitric acid trihydrate (NAT) particles within aqueous nitric acid droplets primarily occurs at the droplet surface. This leads to the hypothesis that phase transformations in atmospheric aerosols may predominantly be surface-based (Tabazadeh et al., 2002b), challenging the traditional theory of homogeneous crystallization where freezing begins inside the volume of the droplet (Volmer, 1939). Satoh et al. (2002) studied cooling and freezing in water droplets due to evaporation in an evacuated chamber and found that droplets rapidly froze with significant supercooling, with the freezing initiated from the droplet surface. Studies employing molecular dynamics simulations (Chushak et al., 1999, 2000) and thermodynamic calculations (Djikaev et al., 2002) additionally corroborate that a crystalline nucleus preferentially forms at the droplet surface rather than within the bulk droplet volume. Laboratory observations from Shaw et al., (2005) reveal that freezing temperatures are 4-5 K higher when an

67 ice-forming nucleus is closer to the surface of a supercooled water droplet compared to when it's immersed within the

68 droplet. They found that the nucleation rate at the water surface is significantly higher (by a factor of 10^{10}) than in the

69 bulk droplet, indicating that the free energy required for critical ice germ formation decreases when near the air-water

70 interface, and the jump frequency of molecules from the liquid to the solid phase may be significantly enhanced at the

71 interface. Lü et al., (2005) conducted ice nucleation experiments with acoustically levitated supercooled water

72 droplets. Using statistical analyses of nucleation rates, they found that ice nucleation predominantly initiates in the

73 vicinity of the droplet surface. Therefore, given the importance of the droplet surface in ice nucleation and since

74 evaporation is a surface phenomenon, in the quest to better understand the physical mechanisms responsible for

75 primary ice nucleation, it is important to accurately investigate the thermal evolution of the evaporating droplet surface

76 as well as the internal thermal gradients within the supercooled droplet, as ice nucleation is highly temperature

77 dependent.

78

79 Droplet condensation or evaporation results from vapor density gradients between the surface of the droplet and the

80 ambient environment. The solution to determine the rate of droplet growth or decay was first derived by Maxwell

81 (1890), with an alternative approximate solution presented by Mason (1971) which has since appeared in several

82 textbooks (e.g. Eq. 7.18 of Rogers and Yau, 1989; Eq. 13-28 of Pruppacher and Klett, 1997). The vapor density at the

83 droplet surface is a sensitive function of the temperature at the drop surface. For simplicity, cloud models, while

84 computing the growth/decay rates of cloud droplets, eliminate the use of droplet temperature from the equations by

85 assuming the saturation vapor density difference as a linear function of temperature difference between the droplet

86 and ambient environment (e.g. Vaillancourt et al., 2001, Chen et al., 2020). This quasi-steady approximation is

87 applicable for droplet growth where the supersaturation is typically less than 1% and the difference between the droplet

88 temperature and ambient air is negligible. For evaporation, where vapor deficits can occur over a wide range of relative

89 humidities, the approximation breaks down as the droplet temperature can deviate significantly from the ambient

90 environment (Srivastava and Coen, 1992; Roy et al., 2023).

91

92 Few studies in the cloud microphysics literature have carried out explicit numerical estimations and evolutions of

93 supercooled, evaporating cloud droplet temperatures and lifetimes for a wide range of environmental conditions. Roy

94 et al., (2023) provides a comprehensive review of past theoretical, numerical, or experimental studies of droplet

95 evaporation. Most of these studies examined the evaporation of raindrops for above 0°C temperatures (Kinzer and

96 Gunn, 1951; Watts 1971; Watts and Farhi, 1975), either assuming steady-state expressions (Beard and Pruppacher,

97 1971) or simplifying assumptions of linear dependence of saturation vapor density on temperature (Kinzer and Gunn,

98 1951; Watts 1971; Watts and Farhi, 1975). Srivastava and Coen (1992) assumed the heat storage term in the droplet

99 heat budget to be negligible, and investigated the evaporation of isolated, stationary hydrometeors by iteratively

100 solving the steady-state solutions, using saturation vapor pressure relations from Wexler (1976) to calculate the

101 saturation vapor density. Roy et al., (2023), by including the heat storage term and solving for time-dependent heat

102 and mass transfer between single, stationary cloud droplets evaporating in infinitely large, prescribed ambient

103 environments, demonstrated that the temperatures of the cloud droplets (initial radii between 30-50 μm) reach steady-

104   state quite quickly (within <0.5 s). They considered a wide range of environmental conditions and found that
105   evaporating droplet temperatures can typically be 1-5 K colder than that of the environment, with values as low as
106   ~10 K for low relative humidity, and low-pressure conditions with near 0°C environments. Their steady-state droplet
107   temperatures agreed well with those of Srivastava and Coen (1992). They showed that the droplet temperature during
108   evaporation can be approximated by the thermodynamic wet-bulb temperature of the ambient environment. For most
109   subsaturated conditions, radiative cooling in cloud-top environments was found to play a negligible role in altering
110   evaporating droplet temperatures, except for larger droplets in environments close to saturation.
111
112   However, two main issues have not yet been accounted for in the aforementioned studies. Firstly, water droplets were
113   considered to have a uniform bulk droplet temperature, based on the assumption of infinite thermal heat conductivity
114   of water, thus ignoring the added complexity of simulating the internal thermal gradients within the droplet. (Kinzer
115   and Gunn, 1951; Watts, 1971; Srivastava and Coen, 1992, Roy et al., 2023). As several studies suggest that the droplet
116   surface plays a special role in nucleating ice and evaporation being a surface phenomenon, accurate modeling of the
117   evolution of droplet surface temperature and internal thermal gradients within the droplet volume is required to
118   correctly predict the ice nucleation rates. Secondly, to date, none of these studies considered the spatiotemporally
119   evolving effects of thermal and moisture feedback between the droplet and its immediate environment. The rationale
120   for justifying the usage of constant ambient conditions far away from the droplet was mostly based on studies where
121   ambient conditions were defined by prescribed temperature and moisture fields far away from a droplet (Sedunov,
122   1974; Eq. 7.7 of Rogers and Yau, 1989; Srivastava and Coen, 1992). A correction to the ambient conditions at a radius
123   similar to the mean distance between droplets (~1 mm) was shown to lead to minimal modifications for typical cloud
124   conditions (Fukuta, 1992). Thus, this assumption holds for droplets distributed homogeneously in space. Concerning
125   numerically simulating the growth and decay of a droplet population, Grabowski and Yang (2013) stated: "Cloud
126   droplets grow or evaporate because of the presence of moisture and temperature gradients in their immediate vicinity,
127   and these gradients are responsible for the molecular transport of moisture and energy between the droplet and its
128   immediate environment. One may argue that these gradients need to be resolved to represent the growth accurately.
129   Elementary considerations demonstrate that the moisture and temperature gradients in the droplet vicinity are
130   established rapidly [i.e., with a characteristic timescale of milliseconds or smaller (e.g., Vaillancourt et al. 2001, and
131   references therein)]; thus, the steady-state droplet growth equation is accurate enough. More importantly, the volume
132   affected by these gradients has a radius of approximately 10 to 20 droplet radii.… One can simply neglect molecular
133   transport processes in the immediate droplet vicinity and simulate droplet growth using the Maxwellian approach, that
134   is, by applying the supersaturation predicted by the mean (over the volume occupied by the droplet) temperature and
135   moisture fields…(see Vaillancourt et al. 2001, appendix)."
136
137   Here, we quantitatively revisit these arguments within the context of an evaporating supercooled cloud droplet. We
138   use high-resolution modeling to resolve the spatiotemporally evolving unsteady thermal and vapor density gradients
139   in the vicinity of the droplet as well as include internal heat transfer within the droplet, relaxing the assumption of
140   infinite thermal heat conductivity of water. Using an advanced numerical model, our framework employs the finite-

141 element method to solve the Navier-Stokes and continuity equations, coupled with heat and vapor diffusion, with

142 appropriate boundary conditions. The results from this study extend the findings from Roy et al. (2023) that an

143 evaporating droplet can exist at a temperature lower than that of the ambient environment, and that the temperature

144 deviation increases from the steady-state value under certain environmental conditions. This may lead to significant

145 enhancement in ice nucleation by increasing the predicted number concentrations of activated ice-nucleating particles

146 (INPs) either immersed within or externally contacting the supercooled droplet. The current study advances the

147 numerical approach presented in Roy et al. (2023) by including the impact of internal heat gradients within the droplet

148 and spatiotemporally varying heat and mass transfer between the droplet and its immediate environment. We also

149 provide droplet lifetime comparisons with estimates from Roy et al. (2023) and pure diffusion-limited evaporation

150 calculations. The implications of the evaporating supercooled cloud droplet temperatures and lifetimes on ice

151 nucleation at cloud boundaries are discussed.

152

2 Numerical Methodology

2.1 Description of COMSOL

155

156 The simulation of the spatiotemporally varying droplet temperature and radius of an evaporating cloud droplet

157 embedded in a gaseous domain is difficult to solve analytically because of the moving and shrinking boundary at the

158 surface of the evaporating droplet. These kinds of moving boundary problems are known as Stefan problems. To

159 model this process, we have used an advanced numerical solver, COMSOL (Version 6.0), which employs a finite

160 element method to solve partial differential equations (PDEs). The COMSOL Multiphysics software simultaneously

161 uses spatial, material, and mesh coordinate systems described as the spatial frame, material frame, and mesh frame,

162 respectively. The spatial frame is a fixed, global, Euclidean coordinate system, which in 2D has spatial cartesian

163 coordinates (r, z) with the center of the droplet at (r, z) = (0,0) (Fig. 1). The material frame specifies the material

164 substance, in this case, water or air. The mesh frame is a coordinate system used internally by the finite element

165 method.

166

167 The Navier-Stokes and Fick's second law of diffusion equation, which follows from the continuity equation, along

168 with appropriate boundary conditions (see Sec. 3) are solved to conserve mass and momentum in the whole system.

169 The following physics interfaces in COMSOL were used to simulate droplet evaporation: (1) *Two-Phase Laminar*

170 *Fluid Flow*, which includes a moving mesh to track the shrinking water–air interface of the evaporating water droplet

171 and fluid–fluid interface that incorporates evaporative mass flux; (2) *Transport of Diluted Species* to track water vapor

172 diffusion through the air domain and predict the evaporation rate at the droplet surface; and (3) *Heat Transfer in Fluids*

173 which accounts for the non-isothermal flow within the computational domain, temperature-dependent saturation vapor

174 density at the droplet interface, and a boundary heat source to account for the latent heat of evaporation. The

175 computational domain also includes an infinite element air domain (COMSOL 2023b) to specify and maintain

176 boundary conditions far away from the droplet. The physics modules are coupled through non-isothermal flow

177   between heat transfer and fluid flow, and mass transport at the fluid–fluid interface between fluid flow and species

178   transport.

179

180   A non-uniform moving mesh was created by breaking down the computational domain into numerous fine elements

181   of variable sizes, using the Arbitrary Lagrangian-Eulerian technique (Yang et al., 2014) to accurately track the moving

182   air-water interface at the droplet surface. In the ALE technique, the spatial cartesian coordinate system (r, z) is fixed,

183   while the coordinates of the material (R, Z) and the mesh (R_m, Z_m) nodes are functions of time as the droplet evaporates.

184   However, the material and mesh node coordinates are always fixed in their respective frames. Initially, the spatial,

185   material and mesh frames are all identical. As the simulation starts, the material and mesh frames deform as the moving

186   boundary of the droplet shrinks during evaporation. After each time step, the deformed nodes are mapped to the spatial

187   frame, where calculations are performed. In this study, we have used triangular mesh elements (COMSOL 2023c)

188   within the droplet and quadrilateral mesh elements (COMSOL 2023d) for the rest of the domain as shown in Fig. 1.

189   The triangular mesh allows a higher resolution at the droplet surface, and both meshes adjust continually as the droplet

190   surface shrinks during evaporation. Finally, to simulate the water droplet evaporating in ambient air system, with

191   appropriate initial and boundary conditions, the discretized PDEs are numerically solved with adaptive time steps (≤

192   0.01 s) to maintain numerical stability and obtain the solution (the temporal evolution of droplet temperature and

193   radius) for a range of conditions.
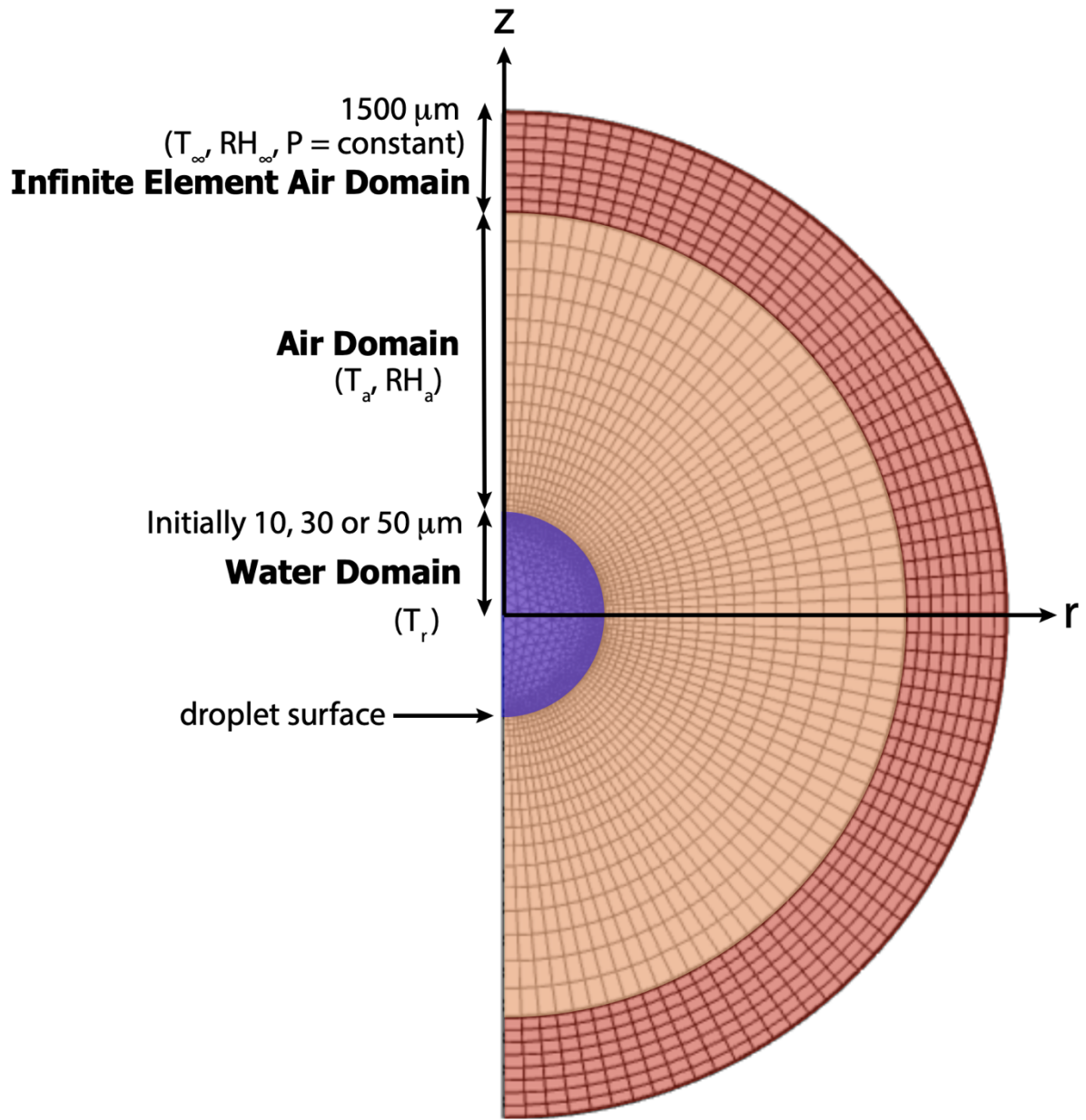
Figure 1: Schematic depicting the evaporating droplet, embedded in the air domain. The spatial frame (r, z) and the initial mesh frame (triangular elements within the droplet and quadrilateral elements outside the droplet) are shown (not to scale).

2.2 Justification for choice of environmental parameters in the simulations

Probing the evolution of the droplet and its immediate environment under a wide swath of conditions was computationally too expensive, thus, certain choices regarding the parameter selection were made. The assumption behind the computational set-up is that the supercooled droplet is suddenly introduced to a subsaturated environment with ambient temperature, T_∞ = 273.15 K, 268.15 K, or 263.15 K, as might happen when the droplets are near cloud boundaries such as those occurring in cloud-top generating cells. These temperatures are the ones where activation of INPs is thought to be least effective. Calculations presented in Sec. 4 consider three different environments having ambient relative humidity, RH_∞ = 10, 40, and 70%, and two different ambient pressures, P = 500, and 850 hPa, and initial cloud droplet radii, r_0, of 10, 30, and 50 μm. The pressure levels were chosen based on the occurrence of 273.15 K, 268.15 K, and 263.15 K in standard atmospheric profiles for tropical latitudes and middle latitudes under warm and cool season conditions (Standard Atmosphere, 2021). Overall, 90 numerical experiments were performed using various combinations of initial RH_∞, T_∞, P, and r_0 to obtain a better understanding of the relationships between the evolution of droplet temperatures and radii, and environmental variables. Of these, the results of 54 experiments are reported in detail herein. The results of these experiments are later summarized in Figs. 3-10 and Tables 1-2. The specific combinations of environmental parameters and initial droplet radii used in this study were also selected to enable easy comparison with results from a previous study of droplet evaporation (Roy et al., 2023). Also, to be noted, the effect of radiation in this study was neglected based on Roy et al. (2023), which demonstrated the negligible role played by radiation in modifying evaporating droplet temperatures under most subsaturated conditions (RH < 80%).

2.3 Justification for choice of droplet lifetime cut-off

For each experiment, the computational time rose exponentially to maintain numerical stability as the droplet radius decreased during evaporation and the grid sizes needed to be smaller. To avoid exceptionally long computation time, the cut-off radius for the simulations was set to be when the volume of the droplets decreased by 99.5% to reach 0.5% of the initial droplet volume. For r_0 = 10, 20, 30, 40, 50 μm, the cutoff radii of the droplets are 1.71, 3.42, 5.13, 6.84, and 8.55 μm, respectively. Note that due to the Raoult effect, for a solution droplet with a mass of dissolved and ionized NaCl = 10^{-13} g, the reduction in the evaporation rate (dr/dt) from that of a pure water droplet is about 1% for a 1 μm radius droplet and 4% for a 0.7 μm droplet. As all cut-off radii considered here are > 1 μm, the solute effect can be neglected. From the Kelvin equation, the equilibrium vapor pressure over a curved surface of pure water approaches the value of equilibrium vapor pressure over a flat surface of pure water for a radius > 0.01 μm. Thus, curvature effects were also neglected. For simplicity, we will refer to the cutoff time as the *droplet lifetime*, although the droplets will survive for a longer time before complete evaporation. The droplet lifetime increases with the initial droplet radius, higher atmospheric pressure, and higher RH_∞ (Fig. 2).
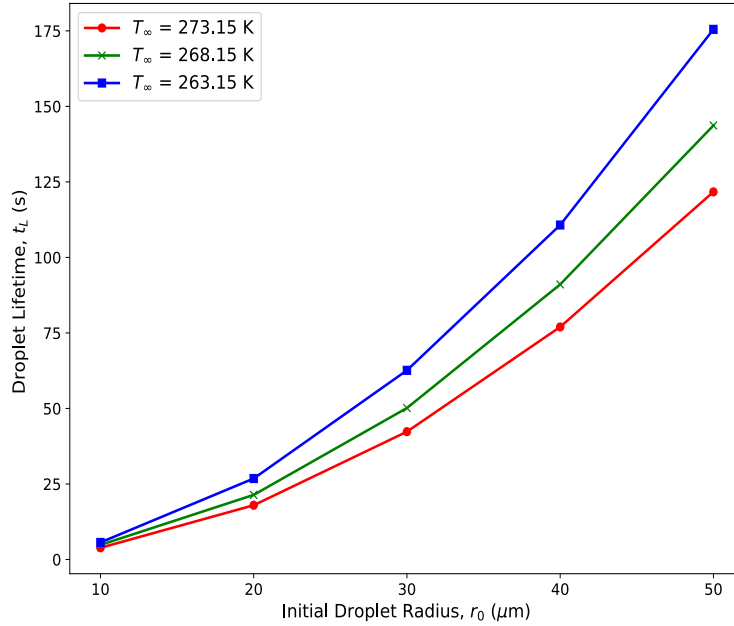
239

240 **Figure 2: Droplet lifetimes, t_L in seconds, for droplets with varying initial droplet radii, r_0 = 10, 20, 30, 40 and 50 μm,**

241 **evaporating in an initial ambient environment with three different ambient temperatures, T_∞ = 273.15 (0°C), 268.15 (-5°C)**

242 **and 263.15 (-10°C) K, with relative humidity, RH_∞ = 70%, with pressure, P = 850 hPa.**

243

244 **2.4 Sensitivity to domain size**

245

246 It was important to ensure that the spatiotemporally varying thermal and vapor density gradients in the ambient air in

247 the vicinity of the evaporating droplet don't interfere with the constant ambient conditions (RH_∞ and T_∞) at the external

248 boundary of the computational domain. Sensitivity tests with different air domain sizes of 10, 30, and 50 times the

249 initial droplet radius were carried out to determine the droplet temperature and radial dependence on domain size. It

250 was found that the evolution of droplet temperature and radius was not sensitive to domain sizes larger than 10 times

251 the droplet radius considered. Based on the sensitivity analysis, the maximum size of the computational domain for

252 all experiments was fixed at 1500 μm, 30 times the largest droplet considered.

253

254 **3 Theory**

255

256 **3.1 Assumptions**

257

258 The framework of the numerical model assumes that an isolated, stationary, spherical, pure water droplet is suspended

259 within a 2D axisymmetric ambient air domain with constant ambient temperature (≤ 0°C) and relative humidity

260 (<100%) at a sufficiently far distance away from the droplet that the droplet evaporation does not influence the far

261 environment. The water droplet and air are considered to be Newtonian fluids, with the assumption that no internal

262 circulation occurs within the droplet and that there is no ventilation, no radiative heat transfer, and negligible buoyancy

263 effects due to gravity. This computational approach is an advanced form of the one described in Roy et al., (2023),

264 but also includes the effect of internal droplet heat transfer and spatiotemporal gradients in temperature and vapor
265 density between the droplet and the environment (see discussion in Sec. 5).
266
267 **3.2 Governing Equations**
268
269 Based on the above assumptions, the following are the equations governing the system during droplet evaporation in
270 the ambient air.
271
272 (1) Fluid flow: The *Laminar Flow* interface models the weakly compressible form of the Navier-Stokes equation,
273 along with the continuity equation in the water and air domains,
274

$$\rho \frac{\partial \boldsymbol{u}}{\partial t} + \rho(\boldsymbol{u}\cdot\nabla)\boldsymbol{u} = \nabla\cdot[-\mathrm{p}\boldsymbol{I} + \boldsymbol{\tau}] + \boldsymbol{F} \tag{1}$$

$$\boldsymbol{\tau} = \mu(\nabla\boldsymbol{u} + (\nabla\boldsymbol{u})^T) - \frac{2}{3}\mu(\nabla\cdot\boldsymbol{u})\boldsymbol{I} \tag{2}$$

$$\frac{\partial \rho}{\partial t} + \nabla\cdot(\rho\boldsymbol{u}) = 0 \tag{3}$$

278
279
280 where t is time, ρ is the fluid density (kg/m^3), $\boldsymbol{u}$ is the fluid velocity vector (m/s), p is pressure (Pa), $\boldsymbol{I}$ is the identity
281 tensor, $\boldsymbol{\tau}$ is the viscous stress tensor (Pa), $\boldsymbol{F}$ is the external volume force vector (N/m^3), which is assumed to be
282 negligible here, and μ is the fluid dynamic viscosity. For water below 273.15 K, the dynamic viscosity can be
283 approximated as 1.79 mPa s. For air, COMSOL uses an empirical equation that produces values equivalent to

284 Sutherland's law (White, 2006), $\mu = \mu_0 \left(\frac{T}{T_0}\right)^{\frac{3}{2}} \left(\frac{T_0 + S_\mu}{T + S_\mu}\right)$ where $\mu_0 = 1.716 \times 10^{-5}$ N s m^{-2}, $T_0 = 273$ K, and $S_\mu = 111$ K

285 for air. The empirical equation is given as:
286 $\qquad \mu = -8.38278 \times 10^{-7} + 8.35717342 \times 10^{-8}T - 7.69429583 \times 10^{-11}T^2 + 4.6437266 \times 10^{-14}T^3 -$
287 $\qquad 1.06585607 \times 10^{-17}T^4$ $\hfill(4)$
288
289 (2) Heat Transport: The *Heat Transfer in Fluids* interface models heat transfer in all domains (air, water, infinite
290 element domain) using the following version of the heat equation:
291

$$\rho C_p \frac{\partial T}{\partial t} + \rho C_p \boldsymbol{u}\cdot\nabla T + \nabla\cdot\boldsymbol{q} = 0 \tag{5}$$

$$\boldsymbol{q} = -k\nabla T \tag{6}$$

294
295 where ρ (kg/m^3) is the fluid density, C_p (J/(kg·K)) is the fluid heat capacity at constant pressure, T is the temperature,
296 k (W/(m·K)) is the fluid thermal conductivity, $\boldsymbol{u}$ (m/s) is the fluid velocity field from the Laminar Flow interface, $\boldsymbol{q}$
297 (W/m^2) is the heat flux by conduction. We chose the value of k for supercooled water at 0.56 W m^{-1} K^{-1} based on Fig.
298 3 of Biddle et al., (2013) where the thermal conductivity of supercooled water is very close to 0.56 W/(m K) for the

299   range of temperatures used in this study. Based on Beard and Pruppacher (1971), the thermal conductivity of air, given

300   by $k_a = 0.004184[5.69 + 0.017(T - 273.15)]$ (W m^{-1} K^{-1}), has very weak dependence on temperature over the

301   temperature range used in this study. For both T = 273.15 K and 253.15 K, the value of k_a is 0.02 W m^{-1} K^{-1}. Hence,

302   we have used a constant value of 0.02 W m^{-1} K^{-1}.

303

304   (3) Mass transport: The *Transport of Diluted Species* interface models water vapor transport through Fick's laws of

305   diffusion, solving the mass conservation equation for vapor transfer in all domains except within the cloud droplet:

306

307
$$\frac{\partial c}{\partial t} + \nabla \cdot \boldsymbol{J} = 0 \tag{7}$$

308
$$\boldsymbol{J} = -D\nabla c \tag{8}$$

309

310   where c is the concentration of water vapor (mol/m^3), D denotes the diffusion coefficient (m^2/s), and $\boldsymbol{J}$ is the mass flux

311   diffusive flux vector (mol/(m^2·s)). D is calculated following Hall and Pruppacher (1976) and defined as follows: $D =$

312    $0.0000211 \frac{P_0}{P} \left[\frac{T}{T_0}\right]^{1.94}$ (m^2 s^{-1}) with reference pressure, $P_0 = 1013.25$ hPa, reference temperature, $T_0 = 273.15\,K$,

313   atmospheric temperature, T, and pressure, P. In this study, values of P are either fixed at 500 or 850 hPa to determine

314   the effect of ambient air pressure on droplet evaporation. $\boldsymbol{J}$ is obtained from the Laminar Flow interface through

315   coupling between these interfaces.

316

317   **3.3 Initial conditions**

318   The initial velocity components in the r, and z directions are assumed to be 0 m/s in both air and water domains. The

319   initial fluid pressure is $p = P_{0,air}$ (Pa), specified either at 500 or 850 hPa in the air domain, and in the water domain, p

320    $= P_{0,water} = \frac{2\sigma}{r_0}$ Pa, where surface tension, $\sigma = 70 \times 10^{-3}$ (N/m). For the heat transfer module, all domains are assumed

321   to be at a prescribed initial ambient temperature, T_0, which is the same as that of a point at a far distance away from

322   the droplet, T_∞.

323   For the vapor transfer interface, except within the droplet, all domains are at an initial vapor concentration of $c_{0,air}$

324   which is again assumed to be the same as that of the constant ambient concentration value far from the droplet, c_∞,

325   calculated as follows:

326    $c_\infty = \frac{RH_\infty \times e_{ST_\infty}}{R_{univ} \times T_\infty}$ where, RH_∞ is set at a constant ambient relative humidity far from the droplet, $R_{univ} = 8.3145$

327   (J/mol/K), T_∞ is in K. The saturation vapor pressure is calculated as, $e_{S\,T_\infty} = 610.94 * \exp\left(\frac{17.625 * T_\infty}{T_\infty + 243.04}\right)$ (in Pa, with

328   T_∞ in °C) following Alduchov and Eskridge (1996).

329

330

3.4 Model Constraints and Boundary Conditions

1. Within the droplet and throughout the domain, the following conditions are applicable:

$$\boldsymbol{u} \cdot \boldsymbol{n} = 0 \tag{9}$$

$$[-\mathrm{p}\boldsymbol{I} + \tau] \cdot \boldsymbol{n} = 0 \tag{10}$$

$$\boldsymbol{q} \cdot \boldsymbol{n} = -k\nabla T \cdot \boldsymbol{n} = 0 \tag{11}$$

$$-D\nabla c \cdot \boldsymbol{n} = 0 \tag{12}$$

where $\boldsymbol{n}$ is the normal to an outward-pointing vector from the center of the droplet. This constraint limits water mass, water vapor and heat flow to the direction normal to the droplet surface.

2. At the fluid-fluid interface i.e., droplet-air boundary, the droplet surface is assumed to be at vapor saturation throughout its lifetime. Hence, saturated vapor concentration at the shrinking droplet boundary, using the ideal gas law, is given by, $c_{sat}(T_{sf}) = \frac{e_s(T_{sf})}{R_{univ} \times T_{sf}}$ where T_{sf} is the surface temperature, in K. The saturation vapor pressure $e_s(T_{sf})$ is estimated as $e_s(T_{sf}) = 610.94 * \exp\left(\frac{17.625 * T_{sf}}{T_{sf} + 243.04}\right)$ (in Pa, with T_{sf} in °C) again following Alduchov and Eskridge (1996).

The local evaporative mass flux at the interface is given by diffusion of water vapor across the water-air interface, M_J (kg/ m^2 s)

$$\boldsymbol{M_J} = M_w \boldsymbol{n} \cdot (-\boldsymbol{D}\nabla \boldsymbol{c}) \tag{13}$$

where the molecular weight of water, $M_w = 0.018$ (kg/mol). Although the temperature is continuous across the droplet-air boundary, there is a discontinuity in heat flux across the interface due to the evaporation of water. Thus, the latent heat of evaporation L, defined as $L = [2501 - 2.44T_r]$ kJ kg^{-1} with droplet surface temperature, T_r in °C, is incorporated as a boundary heat sink as $-M_J L$ (W/m^2).

The mass balance at the water-vapor boundary at the droplet surface, and the velocity of the moving mesh $\boldsymbol{u_{mesh}}$, at the shrinking water-air interface, are expressed by the following equations, based on Scardovelli and Zaleski, (1999):

$$\boldsymbol{u_w} = \boldsymbol{u_v} + M_J\left(\frac{1}{\rho_w} - \frac{1}{\rho_v}\right)\boldsymbol{n} \tag{14}$$

$$\boldsymbol{u_{mesh}} = \left(\boldsymbol{u_w} \cdot \boldsymbol{n} - \frac{M_J}{\rho_w}\right)\boldsymbol{n} \tag{15}$$

where the subscripts w and v represent water and vapor respectively.

The stresses are balanced at the water-vapor interface by the following conditions, based on Yang et al., (2014):

$$n \cdot (S_w - S_v) = \sigma(\nabla_\sigma \cdot n)n - \nabla_\sigma \sigma \qquad (16)$$

$$S = [-pI + \tau] \qquad (17)$$

where S is the total stress tensor and ∇_σ is the surface gradient operator defined by

$$\nabla_\sigma = (I - n \cdot n^T)\nabla \qquad (18)$$

In the normal direction of the boundary, the force is balanced by,

$$n \cdot (S_w - S_v) = \frac{\sigma}{r_c} \cdot n \qquad (19)$$

where r_c is the curvature radius.

3. The external air domain boundary is open with the following condition:

$$[-pI + \tau]n = -f_0 n, \qquad (20)$$

where normal stress, $f_0 = 0$ N/m^2.

4. The infinite element domain consists of air and is considered to be an ideal gas. The temperature, relative humidity, and concentration far from the droplet i.e., at the inner boundary of the infinite element domain, are fixed at T_∞ and c_∞, respectively.

3.5 Coupling between the COMSOL interfaces

To numerically model the evaporating droplet embedded in the air domain, intercoupling between the three physics interfaces - laminar two-phase flow (formulated within the Arbitrary Lagrangian-Eulerian framework), the heat transfer in fluids, and the transport of diluted species within the air medium are established through the following mechanisms: (i) the local evaporative mass flux at the droplet-air interface, which is related to the mesh velocity for the laminar flow, is estimated by the diffusion of water vapor in the air domain; (ii) saturated vapor concentration at the droplet-air interface, which serves as a boundary condition for the vapor diffusion, is calculated using the local temperature at the droplet interface; and (iii) the evaporative heat flux at the droplet-air interface acts as a heat sink boundary condition for the heat transfer in fluids module.

4 Results

Since evaporation is a surface phenomenon, with the evaporative cooling at the droplet surface acting as a heat sink, the temperature of the evaporating droplet surface should be lower than the center of the droplet. In all simulations,

the center to surface temperature gradient within the droplet forms almost instantaneously as evaporative cooling at the droplet surface occurs extremely fast. The time required for the droplet to reach internal thermal equilibrium depended slightly on the initial size of the droplet and the ambient RH_∞, with larger droplets and drier environments leading to more time required by the droplets to reach equilibrium. However, generally, for typical cloud droplet sizes and environmental conditions considered here (r_0 = 10, 30, 50 μm), the internal thermal gradients dissipate and the temperatures throughout the droplets become uniform in ≤ 0.3 s, consistent with Fick's laws of diffusion with a diffusive timescale of r^2/D, where r is the length scale and D is the thermal diffusivity of water. For this study, we have simulated internal droplet heat transfer for the entirety of the droplet lifetime and will be reporting the average droplet temperatures as "droplet temperatures" in the results, unless noted otherwise.

4.1 Droplet Thermal and Radial Evolution: Influence of Initial Droplet Size and Environmental Factors

Figures 3 and 4 depict the early evolution of the droplet average temperatures and radii (r_0 = 10, 30 and 50 μm) for the first few seconds of their lifetimes (as defined in Sec. 2c), for different environments with constant ambient conditions (T_∞, RH_∞, and P) far from the droplet. Tables 1 and 2 provide the final temperature values and total lifetimes of the droplets. Figures 3 and 4 also state the droplet temperatures at the end of their lifetimes (T_L) and the total lifetimes of the droplets (t_L). For all numerical experiments, the evaporating droplet temperature decreases sharply, within < 0.5 s, to a certain temperature defined here as the transition point, T_i, where the slope of the curve changes. After reaching T_i, the decrease in droplet temperature is relatively more gradual as can be seen from Figs. 3 and 4. For example, in Fig. 3(c), for P = 500 hPa, T_∞ = 268.15 K (-5°C), RH_∞ = 10%, a droplet with r_0 = 10 μm, takes about 0.03 s to reach T_i, at 260.98 K (a decrease of 7.17 K from initial temperature). In contrast, a 30 μm droplet takes about 0.12 s to reach T_i, at 260.85 K (a decrease of 7.3 K from initial temperature), and a 50 μm droplet takes about 0.33 s to reach T_i. Finally, the 10 μm droplet reaches the end of its lifetime in 1.05 s i.e. t_L = 1.05 s with temperature, T_L = 244.12 K after reaching T_i, while for the 30 μm droplet, t_L = 11.4 s with T_L = 244.31 K, and t_L = 32.76 s for the 50 μm droplet with T_L = 244.29 K after reaching T_i.

The evaporation process in these experiments starts in a condition that is far from equilibrium. The coupled air- droplet system attempts to evolve towards a steady-state where the thermal energy towards the droplet compensates for evaporative cooling at the droplet surface. In this process, the droplet initially rapidly cools to the thermodynamic wet-bulb temperature of the initial environment similar to what has been shown in Roy et al., (2023). However, under low relative humidity conditions, the thermal and vapor diffusion are not yet near equilibrium. As the system attempts to achieve a steady-state, the imbalance in the heat fluxes associated with vapor and thermal diffusion in the immediate vicinity of the drop leads to a gradual reduction in the wet-bulb temperature of the immediate droplet environment leading to a continued slow decrease in the droplet temperature as the droplet continues to evaporate.

In general, we can see that a higher ambient T_∞, and lower RH_∞ and P leads to a larger reduction in droplet temperature from its initial temperature. Therefore, drier, relatively warmer (closer to 0°C), and lower-pressure environments lead

441   to the strongest evaporative cooling of the droplets. Also, due to evaporative cooling, the droplets survive longer as

442   compared to the pure diffusion-limited evaporation approach where the decreases in evaporating droplet temperature

443   have not been considered (see Sec. 5). However, drier, relatively warmer (close to 0°C), and lower-pressure

444   environments lead to smaller droplet lifetimes as compared to more humid environments, with lower ambient

445   temperatures and higher pressures.

446

447   **4.2 Environmental Evolution: Evolution of Temperature, Relative Humidity, and Wet-Bulb Temperature in**

448   **the air domain near the droplet**

449

450   Figures. 5-7 (a, d) show radial cross sections of the computational domain, starting from the center of the droplet at

451   (r, z) = (0, 0), along the r axis to the edge of the domain at r = 1500 μm, while Figs. 5-7 (b, e) expand the dashed box

452   regions of Figs. 5-7 (a, d), and Figs. 5-7 (c, f) further expand the dashed box regions of Figs. 5-7 (b, e). All panels

453   show the spatiotemporal evolution of temperature (Fig. 5), relative humidity (Fig. 6), thermodynamic wet-bulb

454   temperature (Fig. 7), and droplet radius for a droplet with initial radius, r_0 = 50 μm, introduced to an initial environment

455   with pressure, P = 500 hPa, ambient temperature, T_∞ = 268.15 K (-5°C), with two different relative humidities, RH_∞

456   = 10% and 70%. The evolution of temperature within the droplet is left of the dashed black line, which denotes the

457   droplet radius.

458

459   As the droplet evaporates in the subsaturated domain, evaporative cooling occurs at the droplet surface, leading to

460   heat transfer both from within the warmer droplet and the surrounding air to balance the cooling at the droplet surface.

461   Since the droplet has no constant internal heat source, the internal thermal gradients dissipate quite fast (within 0.3 s)

462   and the average droplet temperatures continue to decrease as the droplet evaporates. Due to heat exchange between

463   the droplet surface and the ambient air in its vicinity, transient thermal gradients in the ambient air develop and lead

464   to a decrease in the air temperature near the droplet. As the droplet shrinks in size along with cooling further, the

465   colder envelope of air surrounding the droplet shrinks as well and the ambient air far from the droplet, at a constant

466   temperature, acts as a heat source and supplies heat to the rest of the domain to attempt to equilibrate the air

467   temperature. Comparing Fig. 5 (a) and (d), at the lower RH_∞, the magnitude of evaporative cooling is much higher.

468   For example, the average temperature of the 50 μm droplet decreases by ~ 10 K in 9 s when RH_∞ = 10%, while the

469   decrease is ~ 5 K in 120 s, when RH_∞ = 70%.
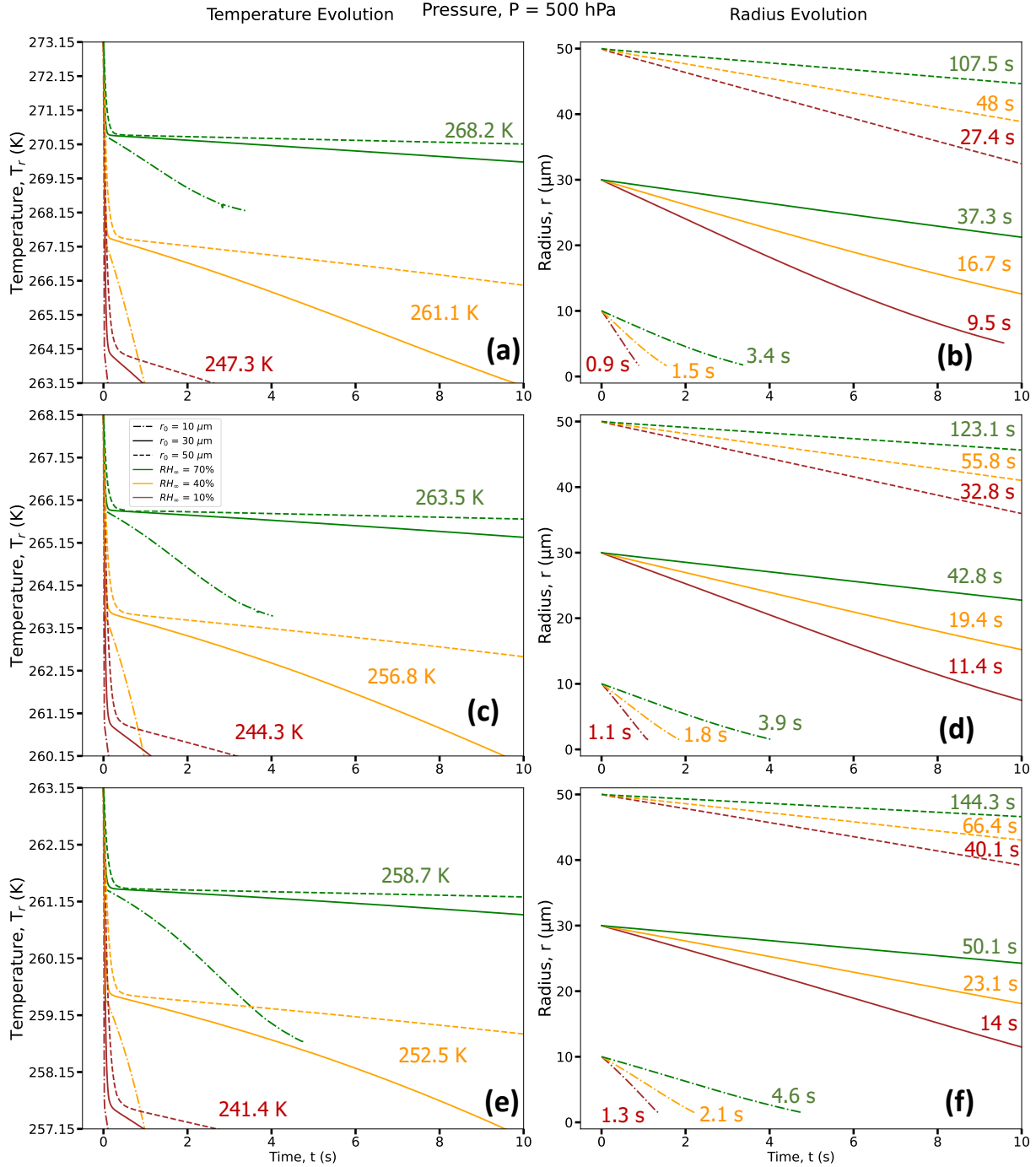
Figure 3: Droplet temperature evolution (left column) and radius evolution (right column) for three different RH_∞ (RH_∞ = 10% (brown curves), 40% (orange curves) and 70% (green curves)), three different r_0 (r_0 = 10 μm (dot-dashed lines), 30 μm (solid lines) and 50 μm (dashed lines)), with three different T_∞ = 273.15 K (0°C) (a, b), 268.15 K (-5°C) (c, d) and 263.15 K (-10°C) (e, f), for P = 500 hPa. For each RH_∞, the average droplet temperature at the end of the lifetimes of the three droplets with different r_0 (T_L, in K) is given in (a,c,e) and the time taken to reach the end of its lifetime (t_L, in s) is given in (b, d, f). Exact values of final temperature for each r_0 are given in Table 1.
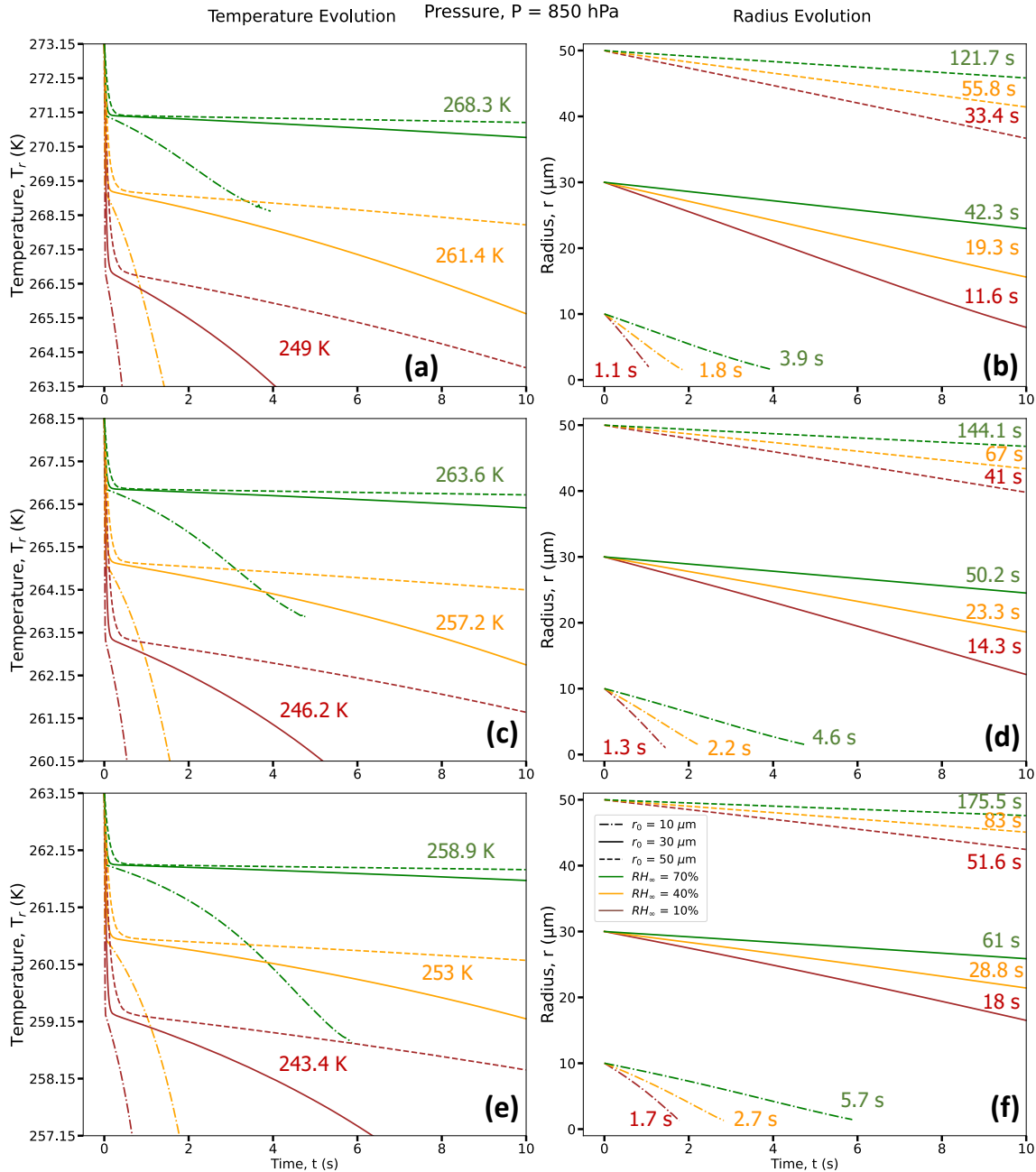
Figure 4: Same as Fig. 3 but for *P* = 850 hPa.

In these simulations, the air in contact with the droplet surface is saturated with respect to water, i.e., *RH* = 100% (Fig. 6, a-f), consistent with assumptions of isolated, stationary evaporating droplets (Kinzer and Gunn, 1951; Srivastava and Coen, 1992). As the water vapor from the evaporating droplet surface diffuses into the surrounding environment, with an initial *RH* (same as RH_∞) of say 10%, vapor density gradients, similar to the thermal gradients, appear and impact the immediate environment of the droplet. These spatiotemporally varying thermal and vapor density gradients play an important role in affecting the droplet temperatures, evaporation rates, and in turn, droplet lifetimes.

487
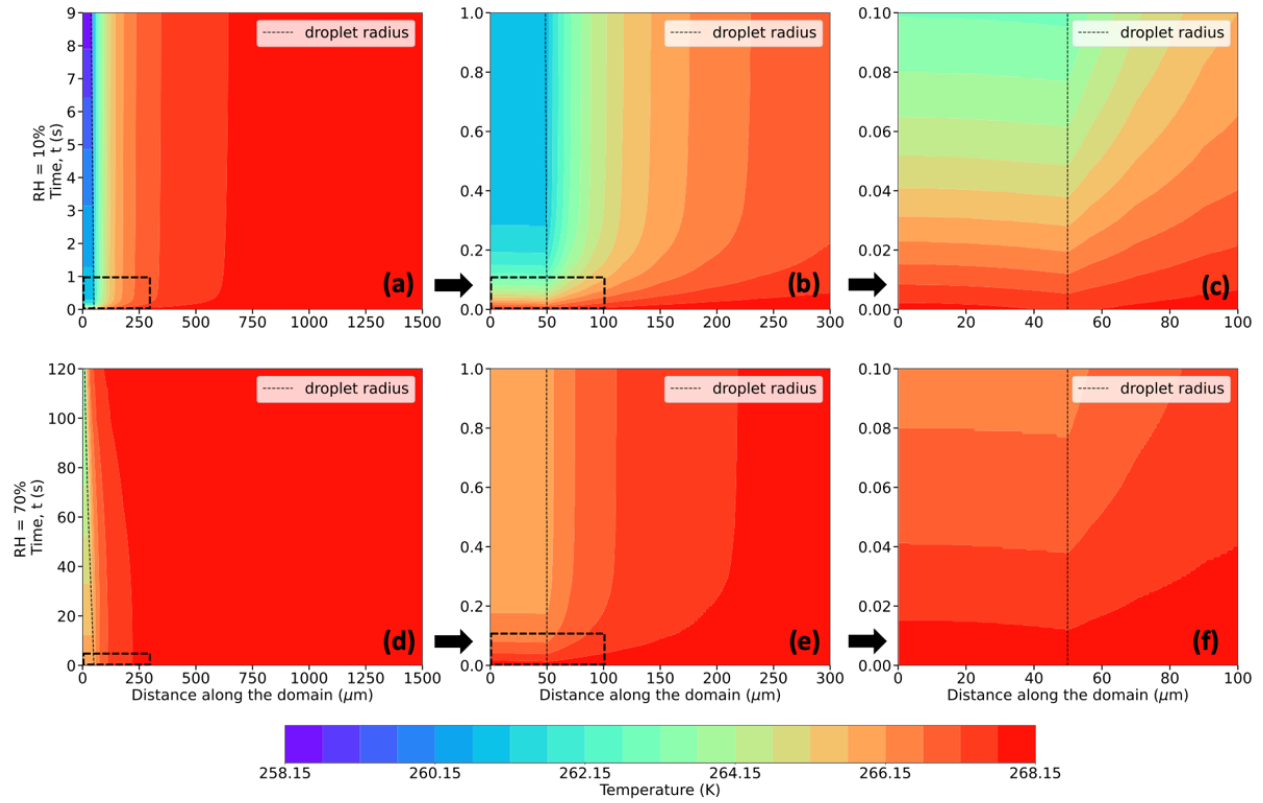
488 **Figure 5: Evolution of temperature (in K, shaded contours), and droplet radius (in µm, dashed black trace) for a 50 µm**
489 **droplet, immersed in an environment with T_∞ = 268.15 K (-5°C), P = 500 hPa, and RH_∞ = 10% (top row) and 70% (bottom**
490 **rows). Bottom left corner of each plot refers to the center of the droplet at (r, z) = (0, 0). Distance along the domain refers**
491 **to the radial distance from the center of the droplet. Figures denoted as (b) and (e), and (c) and (f) present zoomed-in plot**
492 **areas marked by the dashed boxes in (a) and (d), and (b) and (e), respectively.**

493
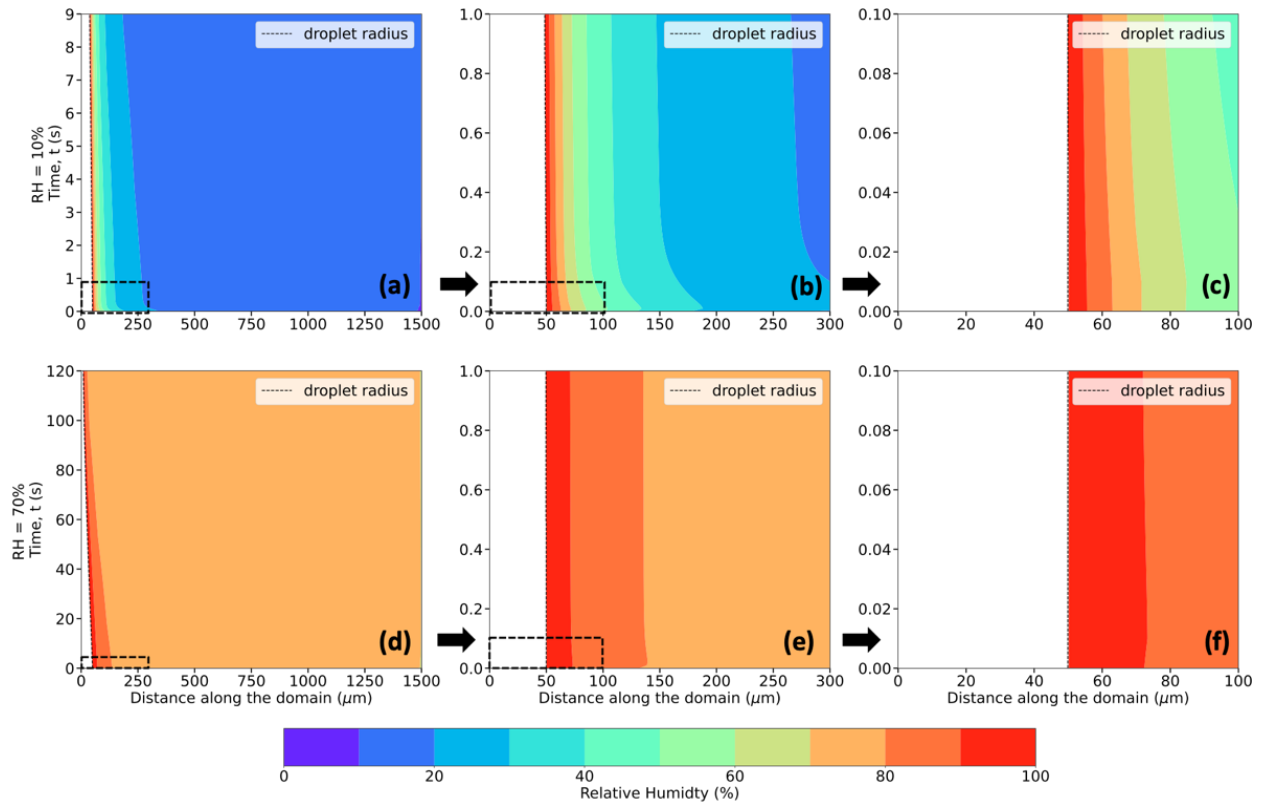
494
495 **Figure 6: Same as Figure 5, but for Relative Humidity (in %, shaded contours), instead of Temperature.**
496

497 Roy et al. (2023) has shown that an evaporating cloud droplet temperature can be well-approximated by the
498 thermodynamic wet-bulb temperature of the environment, especially at higher relative humidities and pressures, and
499 lower ambient temperatures. Following the iterative procedure used in Roy et al. (2023) to calculate the
500 thermodynamic wet-bulb temperature (T_{WB}), Fig. 7 (a-f) depicts the evolution of T_{WB} of the surrounding environment.
501 Unlike previous studies (Srivastava and Coen, 1992; Roy et al., 2023), the ambient environment in this study is not
502 assumed to be spatiotemporally invariant. Hence, as the thermal and vapor density gradients evolve in the ambient air,
503 the T_{WB} of the environment evolves as well, depending on the temperature, relative humidity, and pressure, with the
504 droplet surface temperature the same as that of the T_{WB} of its immediate environment at all times. Of interest, the
505 droplet temperature decreases very quickly to T_i within < 0.5 s (Figs. 3 and 4), which agrees very well with the initial
506 T_{WB} of the surrounding environment and the constant value of the thermodynamic wet bulb temperature far from the
507 droplet ($T_{WB\infty}$). For example, in Fig. 7 (a-c), $T_\infty = 268.15$ K, $P = 500$ hPa, $RH_\infty = 10\%$, $T_{WB\infty} = 261.64$ K, and in Fig. 7
508 (d-f), for $RH_\infty = 70\%$, $T_{WB\infty} = 266.13$ K. Fig. 7 shows the two phases of the evolution of T_{WB} of the immediate
509 environment for two RH_∞ environments – initially, there is a very fast decrease of the air temperature at the droplet
510 surface to $T_{WB\infty}$ typically within < 0.3 s, and then a more gradual decrease of T_{WB} at the droplet surface as the thermal
511 and vapor density gradients in the ambient air become relatively steadier and more established for a period of time,
512 and as their spheres of influence start shrinking as the droplet starts getting smaller in size.
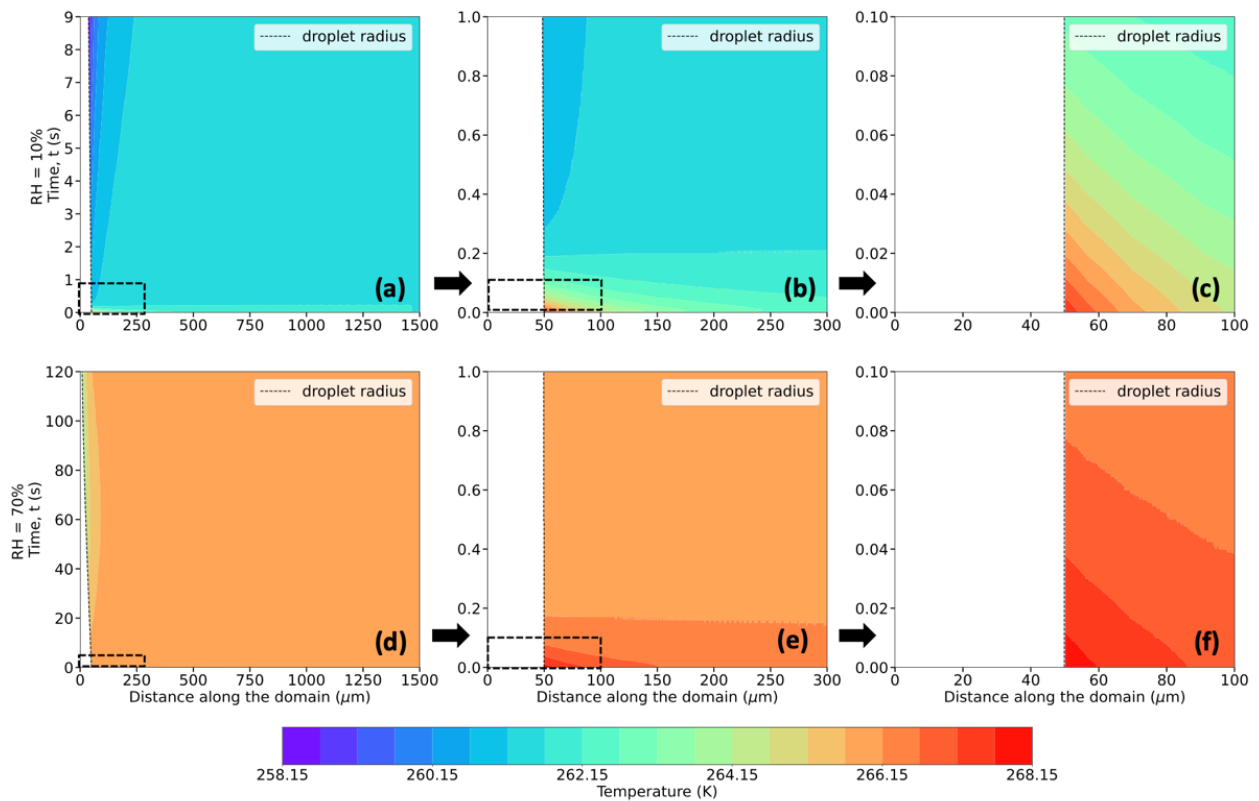
Figure 7: Same as Figure 5, but for thermodynamic wet-bulb temperature (in K, shaded contours).

4.3 Influence of initial droplet size and ambient environmental factors on the thermal evolution of the droplet and its surrounding environment

The overall results spanning the parameter space of the simulations are summarized in Tables 1-2 for the 54 numerical experiments using various combinations of ambient conditions (RH_∞, T_∞, and pressure, P, and r_0) specified at a distance far away from the droplet.

4.3.1 Effect of Ambient Relative Humidity, RH_∞

The decrease in droplet temperature is larger when the RH_∞ is lower due to higher evaporation rates and stronger evaporative cooling under drier conditions. For instance, as shown in Table 1 and Fig. 8 (a, b, c), 30 μm droplets reach ~ 247.3 K (a decrease of 25.8 K from the initial temperature of 273.15 K) for $RH_\infty = 10\%$, ~ 261.1 K (a decrease of 12.1 K) for $RH_\infty = 40\%$ and ~ 268.2 K (a decrease of ~ 5 K) for $RH_\infty = 70\%$. The droplet lifetimes vary depending on RH_∞, with lifetimes increasing with an increase in humidity. For example, the droplet lifetimes for the 30 μm droplet are ~ 9.5 s, 16.7 s, and 37.3 s for environments with $RH_\infty = 10\%$, 40% and 70%, respectively (Table 2). The decrease in droplet temperature and increase in droplet lifetime show similar dependence with increasing RH_∞ for 10 and 50 μm droplets as well.

4.3.2 Effect of Initial Droplet Size, r_0

From Figs. 8-10, for a given initial environmental condition (RH_∞ and T_∞), the droplet temperatures at the end of their lifetimes are independent of the initial droplet sizes. For example, from Table 1 and Fig. 9 (a-i) at $P = 500$ hPa, 10, 30 and 50 µm droplets reach ~ 244 K (a decrease of ~ 24 K from the initial temperature of 268.15 K) for $RH_\infty = 10\%$, ~ 256.8 K for $RH_\infty = 40\%$, and ~ 263.5 K for $RH_\infty = 70\%$. On the other hand, the droplet lifetime strongly depends on the initial droplet size, as the larger droplets take more time to evaporate as compared to the smaller ones. For environments with $RH_\infty = 10\%$, 40% and 70%, the droplet lifetimes for the 10 µm droplet are ~ 1.1 s, 1.8 s, and 3.9 s, while for the 30 µm droplet are ~ 11.4 s, 19.4 s, and 42.8 s, and for the 50 µm droplet are ~ 32.8 s, 55.8 s, and 123.1 s, respectively (Table 2). For a higher pressure of $P = 850$ hPa (Table 1), at the same T_∞, irrespective of r_0, the decrease in droplet temperatures is slightly smaller as compared to $P = 500$ hPa, with values of 22 K, 11 K, and 4.6 K. The radial dependence of the thermal gradients in the ambient air also depends on the initial droplet size, decreasing with a decrease in r_0.

4.3.3 Effect of Ambient Temperature, T_∞

To determine the effect of a lower ambient temperature on droplet temperatures and lifetimes, Figs. 9 and 10 demonstrate similar plots as shown in Fig. 8, but for $T_\infty = 268.15$ K (-5°C) and 263.15 K (-10°C), respectively. The decrease in droplet temperatures and increase in droplet lifetimes depict similar relationships with RH_∞ and r_0. Droplets, irrespective of their initial size, cool to a lower temperature depending on the ambient RH_∞, with the magnitude of the cooling being inversely proportional to the subsaturation of the ambient environment. For instance, for 10, 30 and 50 µm droplets, from an initial temperature of 268.15 K, the droplet temperatures approximately decrease by 24 K, 11.4 K, and 4.7 K, for environments with $RH_\infty = 10\%$, 40%, and 70%, respectively (Table 1). The droplet lifetimes for the 10 µm droplet are ~ 1.1 s, 1.8 s, and 3.9 s, while for the 30 µm droplet are ~ 11.4 s, 19.4 s, and 42.8 s, and for the 50 µm droplet are ~ 32.8 s, 55.8 s, and 123.1 s, for $RH_\infty = 10\%$, 40% and 70%, respectively (Table 2). Comparing these values with those of $T_\infty = 273.15$ K (0°C), it can be noted that a lower ambient temperature leads to a smaller decrease in droplet temperatures and a slight increase in droplet lifetimes in a spatiotemporally evolving environment, for the same RH_∞, r_0 and P. Fig. 10 and Table 1 depict that for $T_\infty = 263.15$ K (-10°C), the reduction in droplet temperatures is slightly smaller, ~ 21.8 K, 10.7 K, and 4.5 K for environments with $RH_\infty = 10\%$, 40%, and 70%, respectively, and droplet lifetimes are longer relative to the higher ambient temperatures of 273.15 K and 268.15 K (Table 2). This is because at a lower ambient temperature, the vapor diffusivity into the ambient air is lower, leading to a weaker evaporation rate with slightly reduced cooling, and extended droplet lifetime, relative to those in an environment with a higher ambient temperature.
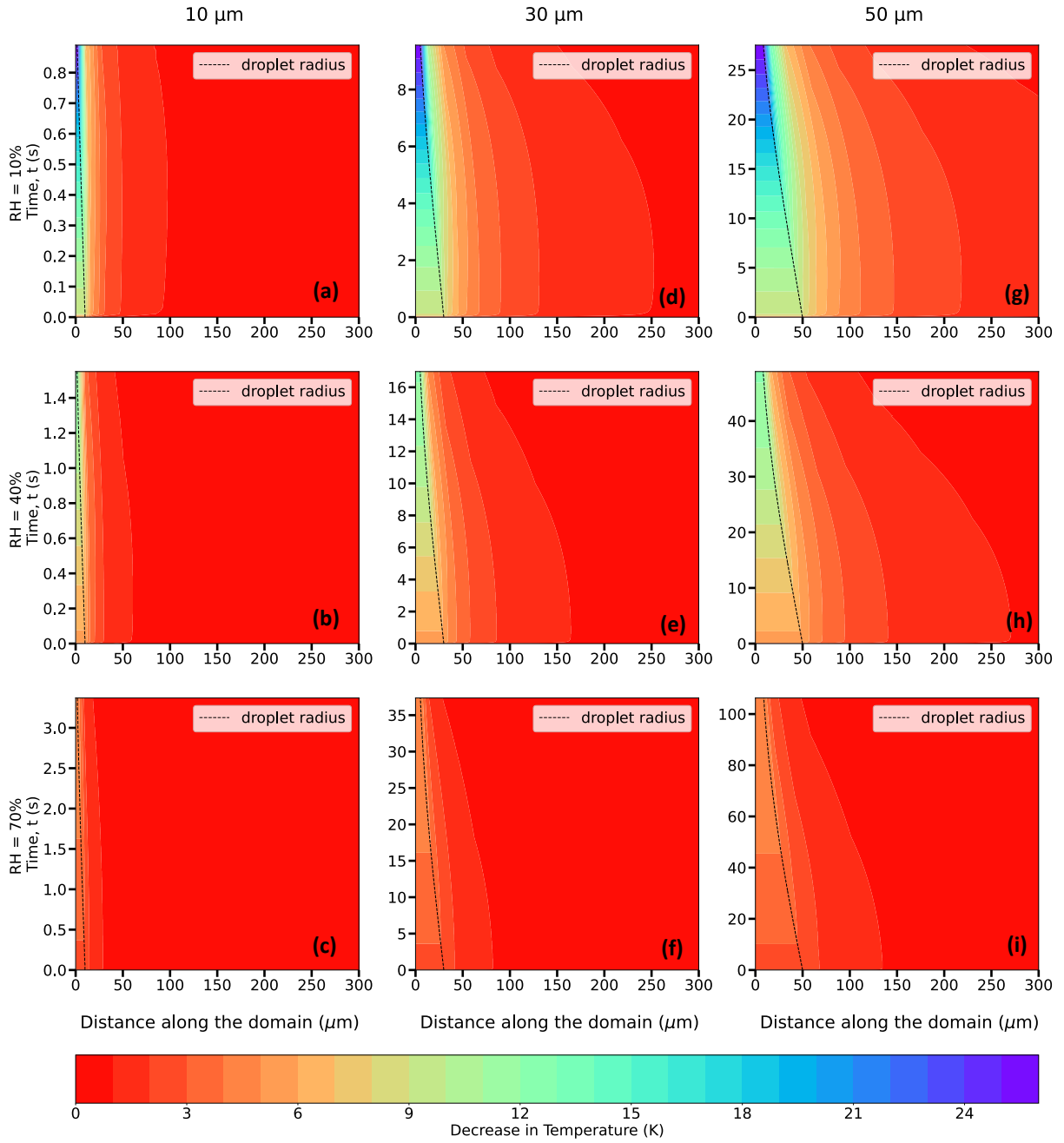
567
568 **Figure 8: Evolution of the decrease in temperature (in K, shaded contours) from the initial temperature of the domain =**
569 **273.15 K (0°C), and of the droplet radius (in μm, dashed black trace) for 10 (a,b,c), 30 (d,e,f), and 50 (g,h,i) μm droplets,**
570 **immersed in an environment with T_∞ = 273.15 K (0°C), P = 500 hPa, and RH_∞ = 10%, 40% and 70%.**
571
572
573
574
575
576
577
578

T_∞ (K)	r_0 (μm)	RH_∞ (%)	$P = 500$ hPa					$P = 850$ hPa				
			$T_{WB\infty}$ (K)	T_{RRD} (K)	T_i (K)	T_L (K)	T_∞-T_L (K)	$T_{WB\infty}$ (K)	T_{RRD} (K)	T_i (K)	T_L (K)	T_∞-T_L (K)
273.15 (0°C)	10	10	264.94	264.06	264.15	247.15	26	267.20	266.49	266.35	249.03	24.12
		40	267.95	267.41	267.35	261.09	12.06	269.30	268.85	268.95	261.40	11.75
		70	270.67	270.43	270.35	268.21	4.94	271.28	271.07	271.10	268.29	4.86
	30	10	264.94	264.06	264.15	247.33	25.82	267.20	266.49	266.37	249.01	24.14
		40	267.95	267.41	267.35	261.08	12.07	269.30	268.85	268.95	261.43	11.72
		70	270.67	270.43	270.45	268.20	4.95	271.28	271.07	271.15	268.26	4.89
	50	10	264.94	264.06	264.15	247.31	25.84	267.20	266.49	266.37	249.04	24.11
		40	267.95	267.41	267.36	261.09	12.06	269.30	268.85	268.95	261.45	11.7
		70	270.67	270.43	270.45	268.20	4.95	271.28	271.07	271.15	268.29	4.86
268.15 (-5°C)	10	10	261.64	260.90	260.98	244.12	24.03	263.57	263.01	263.15	246.32	21.83
		40	263.96	263.50	263.48	256.77	11.38	265.16	264.79	264.82	257.17	10.98
		70	266.13	265.91	265.9	263.47	4.68	266.68	266.51	266.65	263.57	4.58
	30	10	261.64	260.90	260.85	244.31	23.84	263.57	263.01	263.06	246.18	21.97
		40	263.96	263.50	263.46	256.76	11.39	265.16	264.79	264.69	257.18	10.97
		70	266.13	265.91	265.92	263.47	4.68	266.68	266.51	266.56	263.58	4.57
	50	10	261.64	260.90	260.85	244.29	23.86	263.57	263.01	263.06	246.21	21.94
		40	263.96	263.50	263.47	256.76	11.39	265.16	264.79	264.72	257.16	10.99
		70	266.13	265.91	265.92	263.46	4.69	266.68	266.51	266.56	263.56	4.59
263.15 (-10°C)	10	10	258.14	257.55	257.53	241.38	21.77	259.73	259.28	259.28	243.49	19.66
		40	259.89	259.51	259.65	252.46	10.69	260.90	260.60	260.65	252.97	10.18
		70	261.56	261.38	261.4	258.73	4.42	262.04	261.90	261.90	258.88	4.27
	30	10	258.14	257.55	257.62	241.36	21.79	259.73	259.28	259.28	243.27	19.88
		40	259.89	259.51	259.56	252.47	10.68	260.90	260.60	260.54	252.99	10.16
		70	261.56	261.38	261.39	258.73	4.42	262.04	261.90	261.91	258.88	4.27
	50	10	258.14	257.55	257.62	241.37	21.78	259.73	259.28	259.28	243.48	19.67
		40	259.89	259.51	259.56	252.47	10.68	260.90	260.60	260.56	252.99	10.16
		70	261.56	261.38	261.39	258.73	4.42	262.04	261.90	261.91	258.87	4.28

579 **Table 1. Comparison between thermodynamic wet bulb temperatures in the environment far away from the droplet**
580 **($T_{WB\infty}$), simulated droplet steady-state temperatures from Roy et al., (2023) (T_{RRD}), slope transition point temperatures**
581 **(T_i), and droplet temperatures at the end of their lifetimes from this study (T_L), in K, for initial droplet radii, r_0 = 10, 30 and**
582 **50 μm, relative humidities, RH_∞ = 10, 40, 70%, and pressures, P = 500 and 850 hPa, and ambient temperature, T_∞ = 273.15**
583 **K (0°C), 268.15 K (-5°C) and 263.15 K (-10°C).**
584
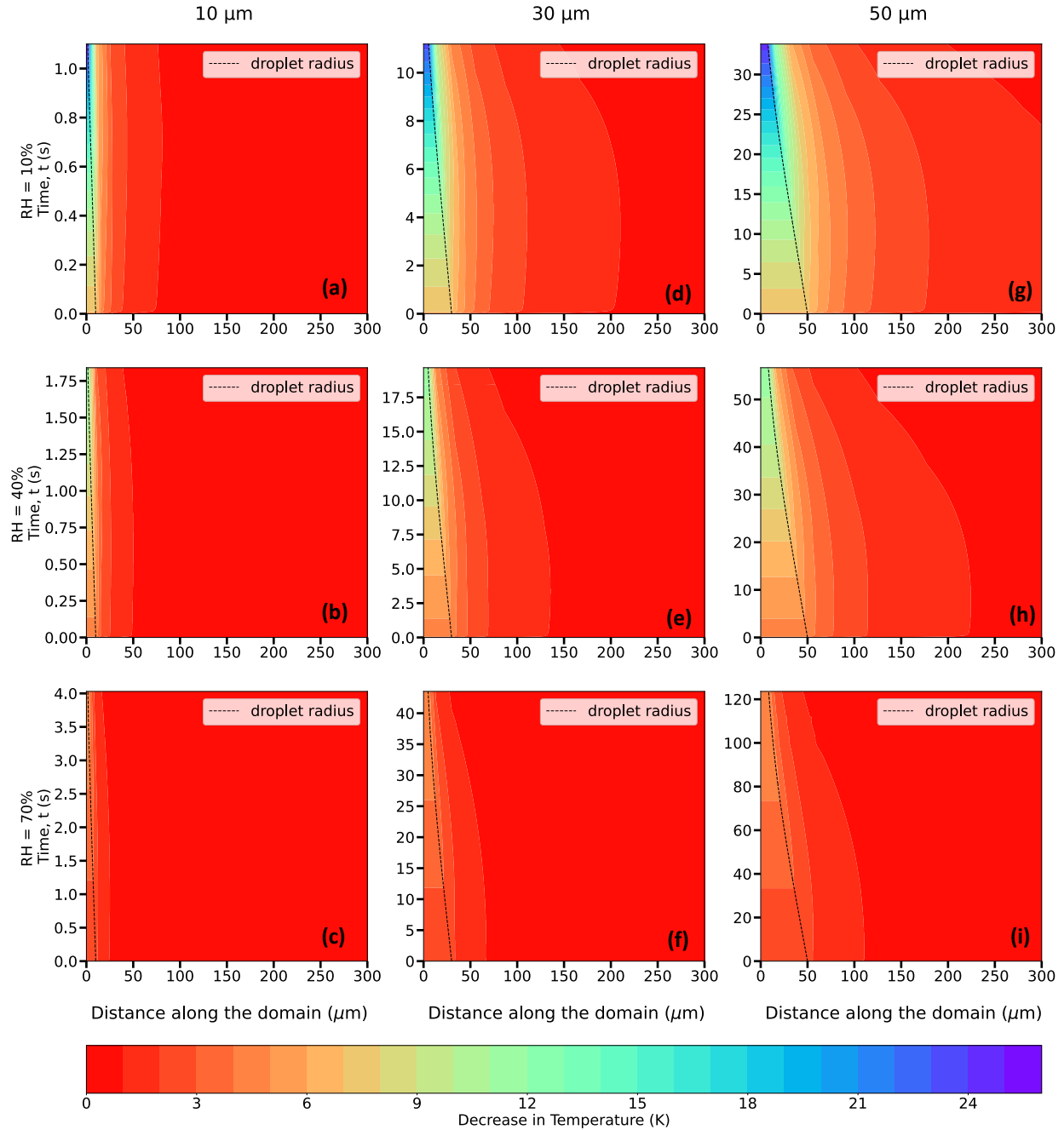
585
586 **Figure 9: Same as Fig. 8 but for T_∞ = 268.15 K (-5°C).**

587
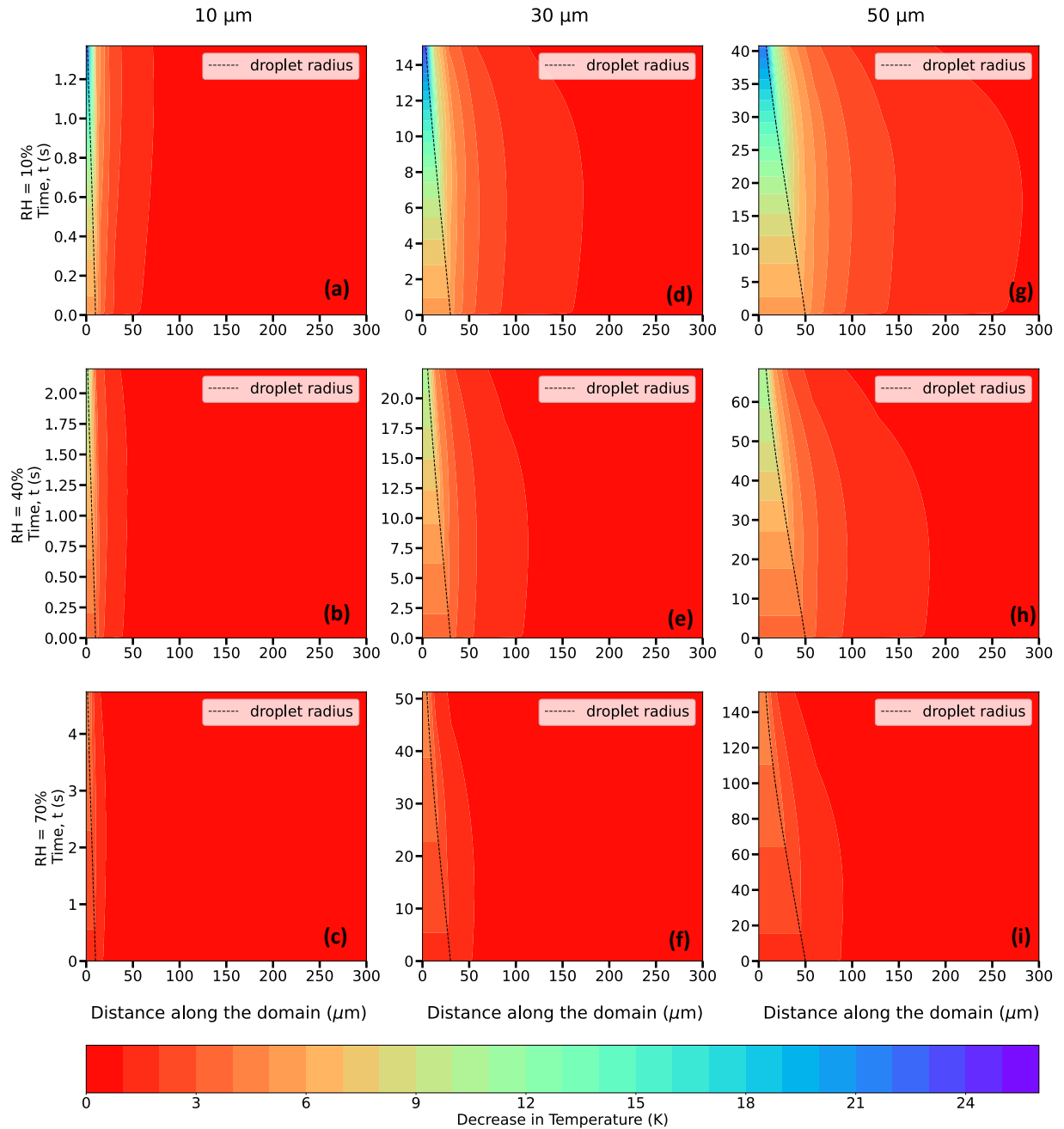
 Figure 10: Same as Fig. 8 but for T_∞ = 263.15 K (-10°C).

590

4.3.4 Effect of Ambient Pressure, *P*

592

The spatiotemporal evolution of the temperature and droplet radius of an evaporating droplet were also investigated

for a higher ambient pressure, *P* = 850 hPa. For a higher pressure, the corresponding decreases in droplet temperatures

are smaller and droplet lifetimes are longer. Under the same environmental conditions but with an increase in ambient

pressure, water vapor diffusivity decreases, leading to a decreased evaporation rate, reduced cooling, and extended

597

T_∞ (K)	r_0 (μm)	RH_∞ (%)	$P = 500$ hPa				$P = 850$ hPa			
			t_{LC} (s)	t_{RRD} (s)	t_L (s)	$\frac{t_L - t_{LC}}{t_{LC}} \times 100\%$	t_{LC} (s)	t_{RRD} (s)	t_L (s)	$\frac{t_L - t_{LC}}{t_{LC}} \times 100\%$
273.15 (0°C)	10	10	0.26	0.56	0.87	234.62	0.44	0.77	1.11	152.27
		40	0.39	0.89	1.51	287.18	0.66	1.18	1.79	171.21
		70	0.78	1.86	3.36	430.77	1.33	2.43	3.87	190.98
	30	10	2.34	5.02	9.54	307.69	3.98	6.84	11.63	192.21
		40	3.51	7.94	16.68	375.21	5.97	10.59	19.33	223.79
		70	7.03	16.73	37.26	430.01	11.95	21.83	42.30	253.97
	50	10	6.51	13.95	27.43	321.35	11.06	19.06	33.35	201.54
		40	9.76	22.08	48.04	392.21	16.59	29.45	55.78	236.23
		70	19.52	46.46	107.45	450.46	33.18	60.64	121.70	266.79
268.15 (-5°C)	10	10	0.38	0.72	1.05	176.32	0.65	1.01	1.32	103.08
		40	0.58	1.12	1.77	205.17	0.98	1.54	2.15	119.39
		70	1.15	2.31	3.91	240	1.96	3.14	4.60	134.69
	30	10	3.45	6.42	11.40	230.43	5.87	9.03	14.27	143.10
		40	5.18	10.01	19.35	273.55	8.81	13.83	23.32	164.70
		70	10.36	20.81	42.79	313.03	17.61	28.25	50.15	184.78
	50	10	9.59	17.88	32.76	241.61	16.31	25.15	40.99	151.32
		40	14.39	27.86	55.76	287.49	24.46	38.48	67.02	173.99
		70	28.78	57.80	123.10	327.73	48.92	78.48	144.07	194.50
263.15 (-10°C)	10	10	0.57	0.95	1.29	126.34	0.98	1.37	1.68	71.43
		40	0.86	1.45	2.13	147.67	1.47	2.08	2.68	82.31
		70	1.72	2.98	4.60	167.44	2.93	4.21	5.66	93.17
	30	10	5.17	8.47	13.95	169.83	8.80	12.28	17.99	104.43
		40	7.76	13.05	23.08	197.42	13.19	18.67	28.83	118.57
		70	15.52	26.79	50.12	222.94	26.39	37.85	61.04	131.29
	50	10	14.37	23.59	40.11	179.12	24.43	34.19	51.59	111.17
		40	21.56	36.30	66.42	208.07	36.65	51.93	82.53	125.18
		70	43.12	74.43	144.33	234.72	73.30	105.16	175.50	139.43

598

599

600 **Table 2: Comparison between different timescales (in sec) in this and other studies, all for the cut off radii used in this**
601 **study. These include droplet lifetimes using the Maxwellian diffusion-limited evaporation approach (t_{LC}), the bulk droplet**
602 **approach in Roy et al., (2023) (t_{RRD}), and as calculated from this study (t_L), for initial droplet radii ($r_0 =$ 10, 30 and 50 μm),**
603 **relative humidities ($RH_\infty =$ 10, 40, 70%), and pressures ($P =$ 500 and 850 hPa), and ambient temperature, $T_\infty =$ 273.15 K**
604 **(0°C), 268.15 K (-5°C) and 263.15 K (-10°C).**
605

606 droplet lifetimes. For example, for an environment with $T_\infty =$ 273.15 K (0°C), $P =$ 850 hPa, 10, 30 and 50 μm droplets

607 reach 249.0 K, 261.4 K, and 268.3 K for $RH_\infty =$ 10%, 40% and 70%, respectively, which are slightly higher as

608 compared to the corresponding droplet temperatures (247.3 K, 261.1 K, and 268.2 K) for $P =$ 500 hPa (Table 1). For

609 higher ambient pressures, droplet lifetimes are also increased due to reduced evaporation rate, with 50 μm droplets

610 now surviving for 33.4 s, 55.8 s, and 121.7 s at $P =$ 850 hPa, instead of 27.4 s, 48.0 s, 107.5 s for $P =$ 500 hPa for RH_∞

611 = 10%, 40% and 70%, respectively (Table 2). Similar trends can also be observed for lower ambient temperatures,

612 268.15 K and 263.15 K, as shown in Table 2.

613

614 **5 Discussion**

615

616 **5.1 Droplet Temperature Sensitivities and Relationship to Thermodynamic Wet-bulb Temperature**

617

618 In these experiments, the droplet temperature initially rapidly decreases to the thermodynamic wet-bulb temperature

619 of the far environment. The novel finding from this study is that the droplet temperature continues to decrease beyond

620 the thermodynamic wet-bulb temperature of the far environment because of the non-equilibrium condition of the

621 thermal and vapor fields during the evaporation process (Fig. 11). The droplet temperature continues to conform to

622 the wet-bulb temperature directly adjacent to the droplet surface, which is lower than the wet-bulb temperature of the

623 far environment. Note that the dependence on T_∞ and P is much smaller than that on RH_∞. The strong dependence on

624 RH_∞ compared to temperature results from the initial conditions. The droplet temperature initially is in thermal

625 equilibrium with its environment (the droplet has the same temperature as that of the far environment), but the vapor

626 field is far from equilibrium, especially for low relative humidity environments. As a result, the vapor diffusion rate

627 (which depends on the vapor density gradient) far exceeds the thermal diffusion rate (which depends on the

628 temperature gradient). Because the cloud droplets are small, and the relative humidity gradients are large, the droplets

629 never come to an equilibrium state before evaporating completely into the subsaturated air. The water vapor flux into

630 the larger subsaturated environment maintains a vapor density near the droplet surface that approaches but never

631 reaches saturation. As a result, the wet-bulb temperature near the droplet surface continues to fall but at a slower rate

632 that depends on RH_∞ (Fig. 11). The pressure affects both the moisture and temperature diffusion fluxes, so these scale

633 with each other, resulting in pressure not having a strong effect compared to that of the moisture gradient.

634
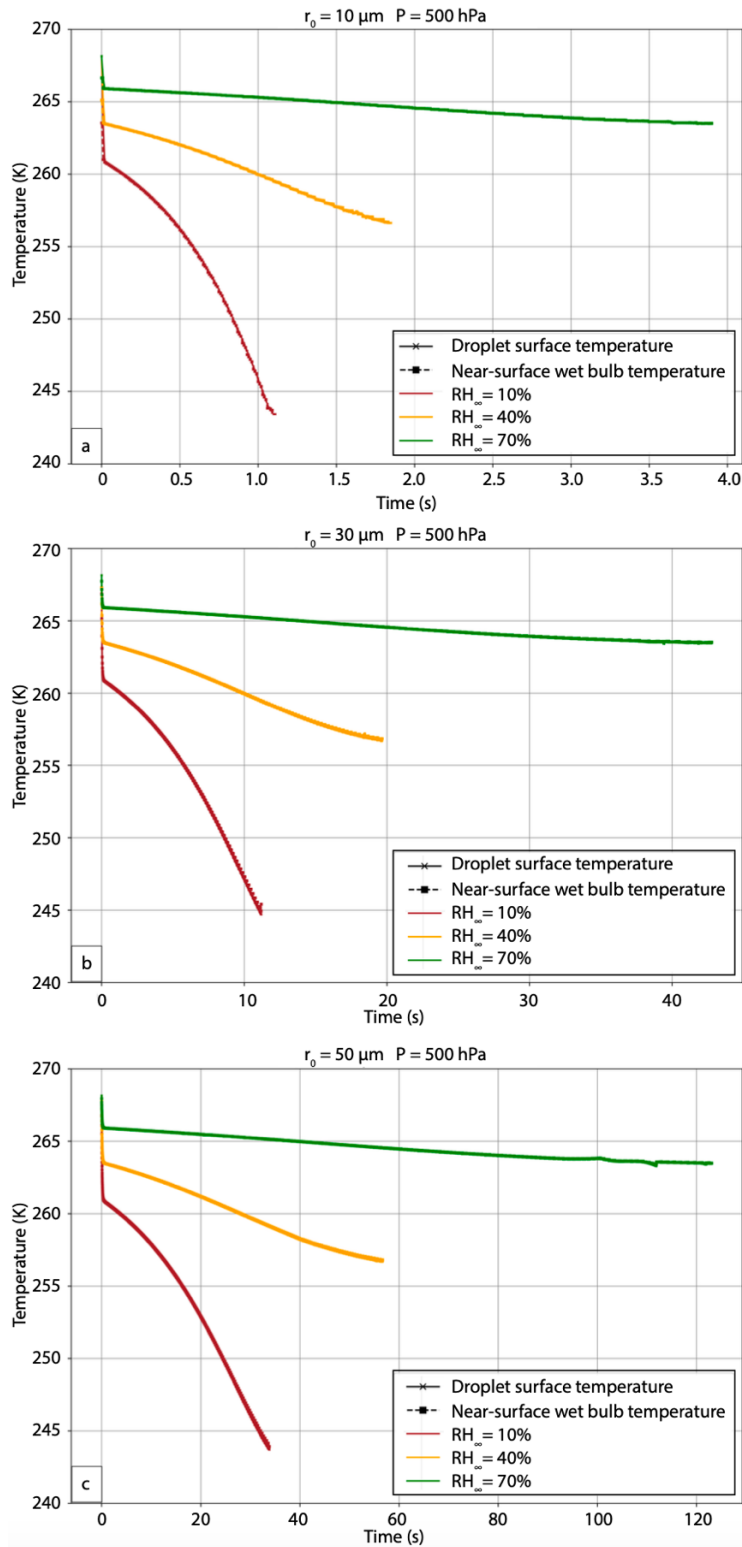
635
636
637 **Figure 11: Evolution of droplet surface temperature (in K, solid lines with cross symbols), and near-surface thermodynamic**
638 **wet-bulb temperature (in K, dashed lines with square symbols) for (a) 10, (b) 30 and (c) 50 μm droplet, immersed in an**
639 **environment with T_∞ = 268.15 K (-5°C), P = 500 hPa, and three different RH_∞. The lines representing droplet surface**
640 **temperature and near-surface thermodynamic wet-bulb temperature essentially overlap.**

5.2 Droplet Temperature and Lifetime Comparison with Previous Studies

As noted in the introduction, not many studies in the cloud microphysics literature have taken a close look at the explicit numerical estimation of supercooled, evaporating cloud droplet temperatures for a wide range of environmental conditions. Previously, a study by Srivastava and Coen (1992) investigated the evaporation of isolated, stationary droplets by iteratively solving the steady-state solutions, using saturation vapor pressure relations from Wexler (1976) to calculate saturation vapor density, and assumed the heat storage terms in the droplet heat budget to be negligible. Roy et al., (2023), solving for time-dependent heat and mass transfer between single, stationary cloud droplets evaporating in infinitely large, prescribed ambient environments, demonstrated that the temperatures of the cloud droplets reach steady-state quite quickly (< 0.3 s). Their steady-state droplet temperatures agreed well with those of Srivastava and Coen (1992) and could be approximated by the thermodynamic wet-bulb temperature of the ambient environment. The current study advances the idealized framework of droplet evaporation as described in Roy et al., (2023) by including the impact of internal heat gradients within the droplet and resolving the spatiotemporally evolving thermal and vapor density gradients between the droplet and its immediate environment to estimate the evaporating droplet temperature and lifetime with higher accuracy.
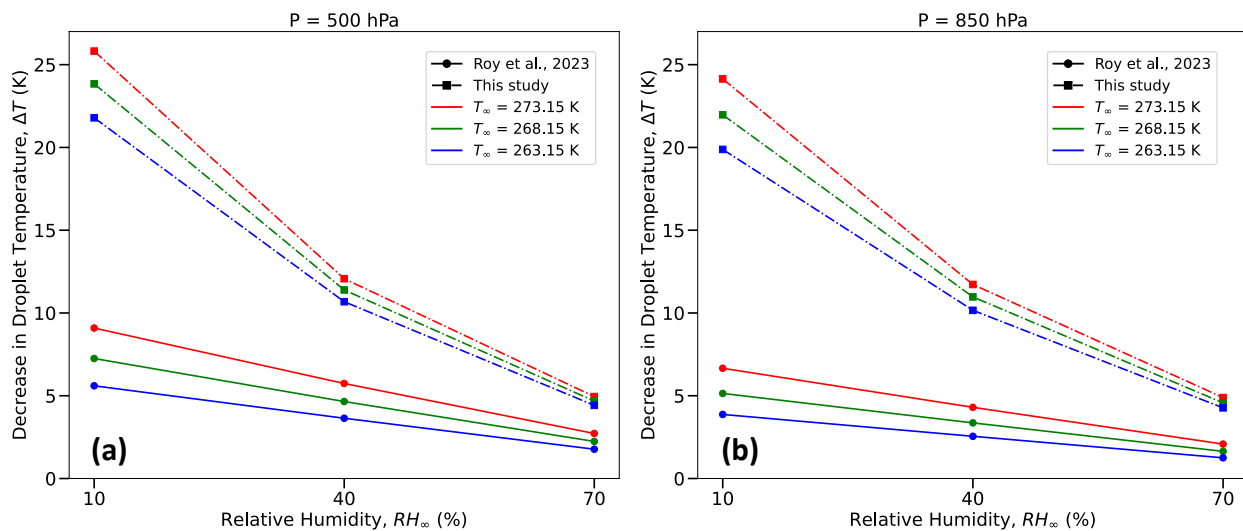
Figure 12: Comparison between the decrease in droplet temperatures (in K) from an initial temperature the same as T_∞, calculated using the bulk droplet model from Roy et al., (2023) (dashed lines), and this study (dashed-dotted lines), for initial droplet radii, $r_0 = 10$, 30 or 50 μm, relative humidities ($RH_\infty = 10$, 40, 70 %), and pressures, $P = 500$ hPa (left column), and 850 hPa right column), and $T_\infty = 273.15$ K (0°C, red), 268.15 K (-5°C, green) and 263.15 K (-10°C, blue).

Table 1 provides a comparison between thermodynamic wet bulb temperatures of the initial environment ($T_{WB\infty}$), simulated droplet steady-state temperatures from Roy et al. (2023) (T_{RRD}), and droplet temperatures at the end of their lifetimes from this study (T_L), in K for several environments. Interestingly, the temperatures at the slope transition point, T_i, as defined in Sec. 3e, are in excellent agreement with $T_{WB\infty}$ and T_{RRD}. In the current study, the droplet temperature continues to decrease almost steadily as the immediate environment in the vicinity of the droplet cools, finally reaching T_L, unlike the evaporating droplet achieving a steady-state temperature in a prescribed ambient environment far away from the droplet in Roy et al., (2023). The evaporating droplet temperature essentially keeps

668 adjusting to the thermodynamic wet-bulb temperature of its immediate changing environment. Therefore, the more
669 realistic simulations of evaporating cloud droplets that include the effect of spatiotemporally varying ambient air
670 thermal and vapor density gradients, as shown in this study, reveal that droplets can potentially achieve even lower
671 temperatures than previously known or estimated from past studies (Srivastava and Coen, 1992; Roy et al., 2023). The
672 decrease in droplet temperatures from their initial temperatures can be much larger, especially for drier environments,
673 as much as 25.8 K for RH_∞ = 10% and 5.0 K for RH_∞ = 70%, for an environment with P = 500 hPa, and T_∞ = 273.15
674 K (Table 1 and Fig. 12a). As shown in Fig. 12, the magnitude of reduction in droplet temperatures decreases with
675 higher ambient RH_∞ and P, and lower T_∞, similar to previous studies (Srivastava and Coen, 1992; Roy et al., 2023).
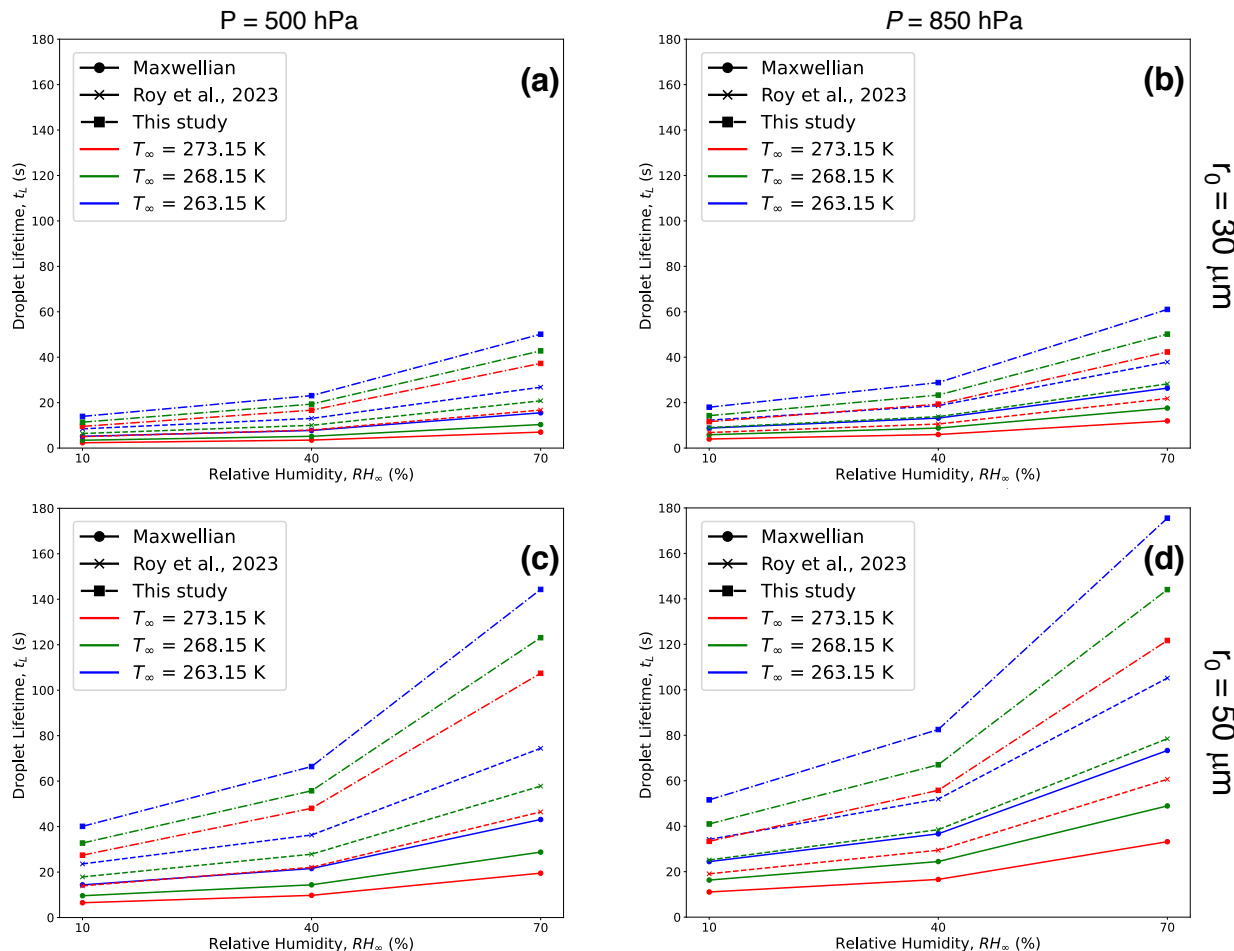
676
677 **Figure 13: Comparison between droplet lifetimes (as defined in this study) calculated using the Maxwellian diffusion-limited**
678 **evaporation approach (solid lines), bulk droplet model from Roy et al., (2023) (dashed lines), and this study (dashed-dotted**
679 **lines), for initial droplet radii, r_0 = 30 μm (upper panel), and 50 μm (lower panel), relative humidities (RH_∞ = 10, 40, 70%),**
680 **and pressures, P = 500 hPa (left column), and 850 hPa right column), and ambient temperature, T_∞ = 273.15 K (0°C, red),**
681 **268.15 K (-5°C, green) and 263.15 K (-10°C, blue). 10 μm droplets (not shown here) have much smaller lifetimes compared**
682 **to 30 and 50 μm droplets.**

683 Table 2 and Fig. 13 provide comparisons between 10, 30 and 50 μm droplet lifetimes (as defined earlier in Sec. 3a)
684 using the Maxwellian pure-diffusion-limited evaporation approach *(t_{LC})*, which ignores evaporative cooling at the
685 droplet surface (Maxwell, 1890; Eq 13-10 of Pruppacher and Klett, 1997*),* the "bulk" droplet approach as described
686 in Roy et al., (2023) *(t_{RRD}),* which ignores internal droplet heat transfer and spatiotemporally varying thermal and

687   moisture gradients in the ambient air, and results from this study (t_L). The magnitude of t_L is greater than the

688   corresponding values of t_{LC} and t_{RRD}. This is because the droplet temperatures in this study never reach steady-state,

689   and are much lower than the corresponding droplet temperatures from the diffusion-limited approach ($\sim T_\infty$), and Roy

690   et al., (2023) ($\sim T_{RRD}$). The greater decrease in evaporating droplet temperature leads to a greater reduction in saturation

691   vapor pressure at the droplet surface. This results in a slower droplet evaporation rate, therefore increasing the droplet

692   lifetime. As shown in Fig. 13, the increase in droplet lifetime depends on the environmental subsaturation, ambient

693   temperatures, and pressures, with a greater increase for more humid, higher pressure, and lower ambient temperature

694   environments. The increase in droplet lifetimes can potentially enhance ice nucleation by increasing the chances of

695   activation of ice nucleating particles (INPs) within the supercooled cloud droplets (see Sect. 5.3).

696

697   **5.3 Implications for ice nucleation**

698

699   Ice nucleation rates are influenced by temperature (Wright and Petters, 2013; Kanji et al., 2017) and time (Vali, 1994).

700   There are two theories in ice nucleation modeling: the time-independent "singular hypothesis," which suggests

701   instantaneous ice formation, and the time-dependent "stochastic hypothesis," which proposes that ice clusters in

702   embryos form and vanish continually, with a frequency that depends on temperature. Supercooled cloud droplet

703   temperatures and their lifetimes are potential contributing factors for the enhancement of ice formation within

704   evaporating regions of clouds such as cloud-tops and edges. As discussed in Roy et al., (2023), evaporative cooling

705   of supercooled cloud droplets in subsaturated environments can enhance ice nucleation near cloud boundaries in two

706   ways: by instantly increasing ice-nucleating particle activation due to lower droplet temperatures (consistent with the

707   singular hypothesis) and/or by extending supercooled droplet lifetimes, allowing more time for nucleation events

708   (consistent with the stochastic hypothesis). Based on limited laboratory investigations available on time dependency

709   of heterogeneous ice nucleation, conducted between temperatures -14 and -30 °C, varying fractions of the droplets

710   were reported to freeze within a range of 1 s to 500 s (Welti et al., 2012; Broadley et al., 2012; Murray et al., 2012;

711   Jakobsson et al., 2022).

712

713   Droplet freezing events can potentially occur within the time frame when the evaporating cloud droplets reach lower

714   temperatures due to evaporative cooling before they completely dissipate into the subsaturated air. This can be seen

715   by comparing the values in Table 2 and Fig. 13 with reported droplet freezing timescales available from experimental

716   studies. Droplet lifetimes as estimated from both approaches (t_{RRD} and t_L), which include droplet evaporative cooling,

717   are longer as compared to the Maxwellian diffusion-limited evaporation approach (t_{LC}), allowing more time for

718   potential occurrence of an ice nucleation event. For temperatures between -5 °C and -10 °C, for the three different

719   subsaturated environments (RH_∞ = 10, 40, and 70%) examined in this analysis, t_{RRD} typically ranged from 0.7 - 4.2 s

720   for 10 μm, 6-38 s for 30 μm and 18-105 s for 50 μm initial radius of droplets, respectively. For similar environments,

721     $t_L > t_{RRD} > t_{LC}$, with t_L typically ranging from 1.1-5.7 s for 10 μm, 11-61 s for 30 μm and 33-176 s for 50 μm initial

722   radii droplets, respectively. For larger droplets, say 30 and 50 μm, the droplets survive much longer as compared to

723   10 μm droplets, likely enhancing the chances of an ice nucleation event.

724

725 Results from this study further strengthen evidence of the hypothesized mechanism of enhancement of ice nucleation

726 via droplet evaporation. Together with the consistent observation of supercooled water in cloud-top generating cells

727 (Plummer et al., 2014; Zaremba et al., 2024), these results contribute to explaining the observations of the prodigious

728 production of ice particles produced in generating cells at the cloud-tops of winter storms and other clouds (e.g.,

729 Plummer et al., 2015, Wang et al., 2020). Rauber et al. (1986), Plummer et al. (2015), and Tessendorf et al. (2024)

730 have shown that cloud droplet concentrations at the generating cell level near cloud-tops are of the order of 30-50 cm$^-$

731 ^{3}, while ice-particle concentrations in the plumes of ice particles falling beneath generating cells are of the order of

732 0.01 cm^{-3}. Based on these values, if less than one frozen cloud droplet in 1000 survive sublimation after freezing and

733 fall back into the cloud, that would be sufficient to create the ice-particles observed falling from a generating cell.

734

735 Due to the observational evidence of a higher dependency of ice nucleation on temperature than time (Wright and

736 Petters, 2013), and the increased difficulty of representing time-dependent stochastic nucleation in numerical models,

737 the simpler and more widely used approach is to use the time-dependent singular hypothesis framework to simulate

738 ice initiation processes. Drawing from theoretical insights, laboratory experiments, and field campaigns, numerous

739 parameterization methods for modeling heterogeneous ice nucleation in cloud and climate models have been created

740 over the years (Fletcher, 1962; Cooper, 1986; Meyers et al., 1992; DeMott et al., 1998; Khvorostyanov and Curry,

741 2000; Phillips et al., 2008). Most of the conventionally used schemes (Fletcher, 1962; Cooper, 1986; Demott et al.,

742 2010) share a common feature, which is the utilization of the ambient air temperature for estimating activated INPs,

743 as opposed to relying on the droplet temperature, even for primary ice-nucleation modes such as immersion freezing

744 and contact nucleation.

745

746 Similar to Roy et al. (2023), we investigate the maximum enhancement in activated INP concentrations that can occur

747 due to evaporative cooling of supercooled water droplets in a spatiotemporally varying environment, assuming that

748 the activation in the parameterization schemes (Fletcher, 1962; Cooper, 1986; Demott et al., 2010) is related to the

749 droplet temperatures towards the end of their lifetimes (T_L) rather than the ambient temperature. Fig. 14 presents a

750 comparison between Roy et al. (2023), and the current study in terms of the highest fractional increase in activated

751 ice-nucleating particles (INPs), as projected through the Fletcher, Cooper, and Demott schemes (considering ambient

752 aerosol concentration, N_a, with diameters greater than 0.5 μm). Owing to even lower droplet temperatures during

753 evaporation, the fractional increase in activated INPs is higher as calculated from this study, with several orders of

754 magnitude increase for drier environments. For example, the Fletcher Scheme predicts an enhancement in activated

755 INPs by a factor of ~10^6 for $RH_\infty = 10\%$, $T_\infty = 268.15$ K, $P = 500$ hPa based on droplet temperatures from this study,

756 while the corresponding number from Roy et al. (2023) is ~100 (Fig. 14a). The fractional increases are slightly smaller

757 for higher pressure environments due to lower evaporative cooling of the droplets under such conditions (compare

758 Figs. 14a, d, b,e, and c,f). Consistent with previous results from Roy et al. (2023), compared to the Fletcher Scheme,

759 the Cooper and Demott schemes demonstrate relatively lower enhancement in activated INPs. For the same

760   environment stated earlier, the corresponding activated INP enhancement factor values for Cooper and Demott

761   schemes are ~10^3 and 80, respectively (Figs. 14b and c).

762

763   Therefore, results from the current study further corroborate the hypothesized ice nucleation enhancement mechanism

764   through evaporative cooling of supercooled droplets (Mossop et al., 1968; Young, 1974; Beard, 1992; Roy et al.,

765   2023), providing much higher estimates of activated INP concentrations from previous analyses (Roy et al., 2023).

766   This potential increase in INP concentrations in subsaturated environments near cloud tops and edges, particularly at

767   higher sub-freezing temperatures, may partially help resolve the several orders of magnitude discrepancy between

768   predicted INP and observed ice particle concentrations in such regions of the cloud. To evaluate the effectiveness of

769   the potential ice-nucleation enhancement mechanism through evaporation, future modeling experiments within a

770   robust dynamical model setup, considering a population of both freezing and evaporating droplets, along with their

771   lifetimes, droplet-droplet interaction, different species of INPs, and the impact of turbulence and other feedbacks, are

772   required.
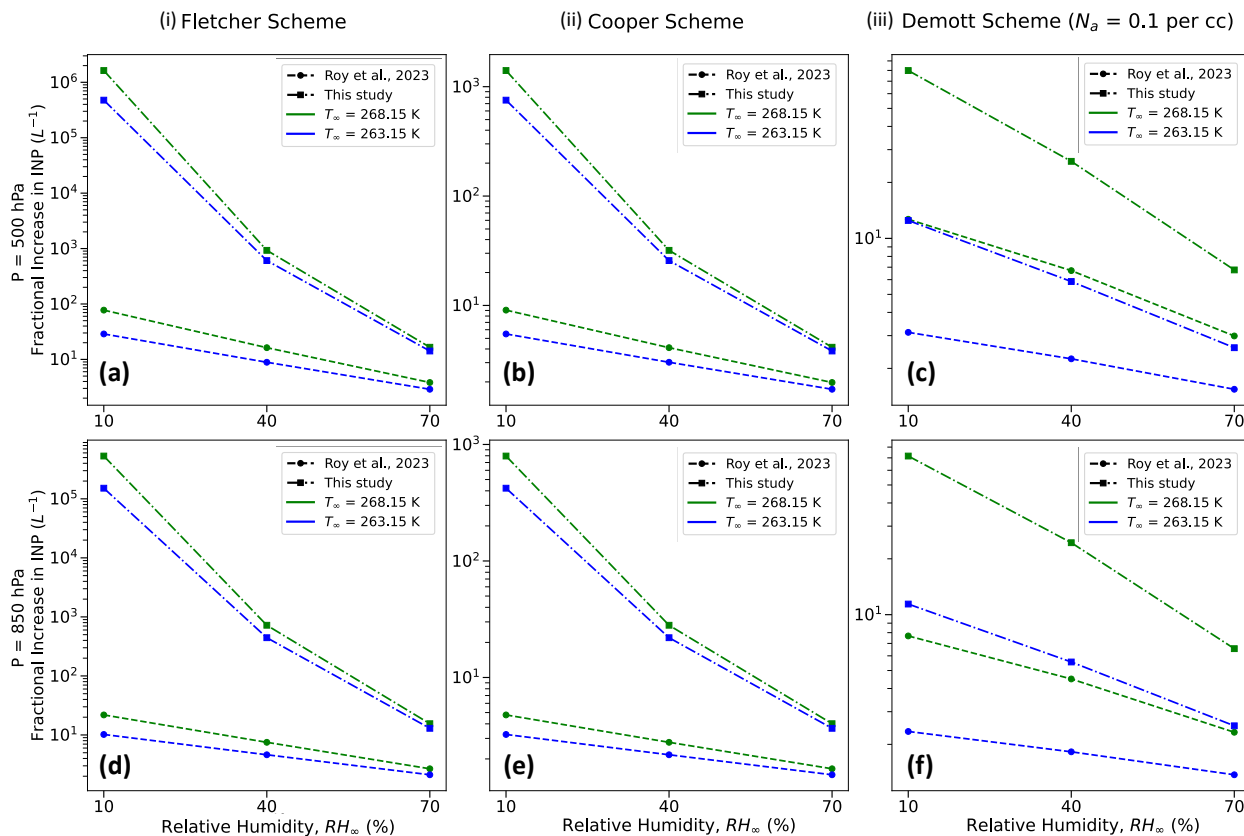
773

774   **Figure 14: Comparison between the maximum fractional increase in INPs as estimated by Roy et al., (2023) and this study**

775   **for three different parameterization schemes: (i) Fletcher (1962) (ii) Cooper (1986), and (iii) Demott et al., (2010), for three**

776   **different environmental relative humidities (RH_∞ = 10, 40 and 70%), and two ambient temperatures (T_∞ = 268.15 K (-5°C)**

777   **and 263.15K (-10°C)) and two different pressures (P = 500 and 850 hPa).**

778

779

780

6 Conclusions

In this study, we presented a quantitative investigation of the temperature and lifetime of an evaporating droplet, considering internal thermal gradients within the droplet as well as resolving spatiotemporally varying unsteady thermal and vapor density gradients in the surrounding ambient air. The computational approach involved solving the Navier-Stokes and continuity equations, coupled with heat and vapor diffusion equations, using an advanced numerical model that employs the finite element method. This is the first simulation of the spatiotemporal evolution of droplet temperature, radius, and its environment for an isolated, stationary, and supercooled cloud droplet evaporating in various subsaturated environmental conditions. Various ambient pressure (P), temperature (T_∞), relative humidity (RH_∞), and initial droplet radii (r_0) were considered. The motivation behind this study was to provide more exacting calculations to support the hypothesized ice nucleation enhancement mechanism due to the evaporation of supercooled cloud droplets at cloud boundaries, such as cloud-top ice-generating cells, and for ambient temperatures between 0°C and -10°C where ice nucleation is least effective.

The numerical simulations show for typical cloud droplet sizes (r_0 = 10, 30, 50 μm) and environmental conditions considered here, the internal thermal gradients dissipate quite quickly (≤ 0.3 s) when the droplet is introduced to a new subsaturated environment. Thus, spatial thermal gradients within the droplet can be reasonably ignored. Hence, one can potentially ignore the extra computational expense of simulating conductive heat transfer within the droplet for timescales > 1 s.

The results from this study are similar to findings from the literature that an evaporating supercooled cloud droplet can exist at a temperature lower than that of the ambient atmosphere and that the tendencies of the dependence of decrease in droplet temperatures on environmental factors and initial droplet sizes (Srivastava and Coen, 1992; Roy et. al, 2023). The novelty of this study lies in demonstrating that the magnitude of droplet cooling can be much higher than estimated from past studies of droplet evaporation, especially for drier environments. For example, a droplet evaporating in an environment with P = 500 hPa, T_∞ = 268.15 K (-5°C), RH_∞ = 10%, Roy et al., (2023) estimated a 7.3 K decrease in droplet temperature, while this study shows that there can be as much as a 23.8 K decrease in droplet temperature. This is because previous studies assumed prescribed ambient environments at all distances from the droplet, while this analysis shows that as a droplet evaporates and cools, the air in the vicinity of the droplet cools as well, giving rise to spatiotemporally varying thermal and vapor density fields in the immediate environment surrounding the droplet. Here, the net conductive warming from the environmental air enveloping the droplet is lower as compared to Roy et al., (2023), effectively leading to a much lower droplet temperature. At a particular time, the strength and radial dependence of these gradients depend on the subsaturation of the air medium and the magnitude of droplet cooling due to evaporation, with the largest cooling at lower RH_∞. In this study, the temperature and vapor density in the ambient air continually evolve, thus affecting the transfer of heat and vapor between the droplet surface and the environment far away from the droplet. This affects the temperature evolution and decay rates of the

817   evaporating droplet to a greater degree than shown in previous studies for a similar environment (Srivastava and
818   Cohen, 1992; Roy et al. 2023).

819

820   This study also demonstrated that the lifetimes of the evaporating droplets are longer compared to Roy et al. (2023)
821   because as the droplet temperature gets lower, the saturation vapor pressure at the droplet surface reduces, leading to
822   a weaker evaporation rate. For an environment with $P = 500$ hPa, $T_\infty = 268.15$ K (-5°C), $RH_\infty = 10\%$, a 50 μm droplet
823   reaches the end of its lifetime, as defined in this study, in 32.8s, while the corresponding values for the diffusion-
824   limited evaporation approach as estimated from Roy et. al, (2023) are 9.6 s and 17.9 s, respectively. The rates of
825   evaporation tend to be lower in this study due to even lower droplet temperatures as well as spatiotemporally varying
826   vapor density gradients around the droplets. As the droplet evaporates, the envelope of air surrounding the droplet is
827   colder, has lower values of diffusivity leading to lower evaporation rates, and has higher vapor concentration than the
828   ambient air, thus decreasing the evaporation rates.

829

830   To summarize, if one considers the more realistic case of droplet evaporation, including the spatiotemporally varying
831   thermal and vapor density gradients in the vicinity of the water droplet, the evaporating droplet can experience a
832   substantial reduction in temperatures by several degrees, strongly dependent on the ambient relative humidity and
833   weakly dependent on ambient pressure and temperature. Similar to the case of an isolated, stationary droplet
834   evaporating in a prescribed ambient environment, the droplet almost immediately reaches its slope transition point
835   temperature, which can be well-approximated by the thermodynamic wet-bulb temperature of the initial ambient
836   environment around the droplet. Droplet temperatures then continue to steadily decrease as they adjust to the evolving
837   thermodynamic wet-bulb temperature of the surrounding air. In more humid environments, the droplets may not
838   experience a larger droplet cooling, but their lifetimes, as defined in this study, get extended by tens of seconds as
839   compared to the Maxwellian estimation which neglects droplet cooling.

840

841   The current analysis also demonstrates that lower evaporating droplet temperatures would lead to an enhancement of
842   activated INPs from three widely used INP parameterization schemes, further corroborating the hypothesized ice
843   nucleation enhancement mechanism through evaporative cooling of supercooled droplets. Notably, the estimates of
844   activated INP concentrations from this study are higher than previous analyses, as the droplet temperatures are much
845   lower towards the end of their lifetimes, with several orders of magnitude increase in activated INPs for drier
846   environments. The Fletcher Scheme predicts the greatest enhancement in activated INPs by a factor of ~10^6 for RH_∞
847   = 10%, $T_\infty = 268.15$ K, P = 500 hPa, while the corresponding enhancement factor values for Cooper and Demott
848   schemes are ~10^3 and 80, respectively.

849

850   This study suggests a need for a more in-depth examination of supercooled cloud droplet temperatures and their
851   lifetimes in subsaturated environments, especially when simulating heterogeneous ice nucleation processes that
852   require the presence of supercooled water droplets. This is crucial because the concentration of activated ice-
853   nucleating particles (INPs) is influenced by both droplet temperature and how long evaporating droplets persist.

Additionally, the findings from this investigation may also partially help understand disparities between observed ice particle concentrations and activated INPs, especially at relatively higher sub-0°C temperatures. Including the effect of droplet evaporative cooling on droplet temperatures and lifetimes, while modeling cloud microphysical processes in subsaturated environments, will also lead to improved accuracy of the evolution of the droplet size distribution as well as primary ice nucleation mechanisms.

Author contribution: PR, RMR and LDG conceptualized the problem and numerical experiments. PR designed and performed the simulations, analyzed the data, and prepared the first draft of the manuscript. RMR and LDG reviewed and edited the manuscript. RMR and LDG acquired required funding for the project.

Competing interests: The authors have no competing interests.

Acknowledgements: This work was funded by the NASA CAMP^{2}Ex program under grant 80NSSC18K0144 and the NASA Earth Venture Suborbital-3 (EVS-3) IMPACTS program under grant 80NSSC19K0355. This research was also supported by the National Science Foundation under grant NSF AGS-2016106.

Code/Data availability: This modeling analysis used the proprietary COMSOL Multiphysics version 6.0 software package which can be licensed through https://www.comsol.com/.

References

Alduchov, O.A. and Eskridge, R.E.: Improved Magnus form approximation of saturation vapor pressure, Journal of Applied Meteorology and Climatology, 35(4), pp.601-609, https://doi.org/10.1175/1520-0450(1996)035<0601:IMFAOS>2.0.CO;2, 1996.

American Meteorological Society (AMS 2024): Generating cell. https://glossary.ametsoc.org/wiki/Generating_cell (Last accessed May 10, 2024)

Beard, K.: Ice Initiation in warm-base convective clouds: An assessment of microphysical mechanisms, *Atmos. Res.,* 28, 125-152, https://doi.org/10.1016/0169-8095(92)90024-5, 1992.

Biddle, J.W., Holten, V., Sengers, J.V. and Anisimov, M.A.: Thermal conductivity of supercooled water. *Physical Review E*, *87*(4), p.042302, https://doi.org/10.1103/PhysRevE.87.042302, 2013.

Broadley, S.L., Murray, B.J., Herbert, R.J., Atkinson, J.D., Dobbie, S., Malkin, T.L., Condliffe, E. and Neve, L.: Immersion mode heterogeneous ice nucleation by an illite rich powder representative of atmospheric mineral dust, Atmospheric Chemistry and Physics, 12(1), pp.287-307, https://doi.org/10.5194/acp-12-287-2012, 2012.

Chen, S., Xue, L. and Yau, M.K.: Impact of aerosols and turbulence on cloud droplet growth: an in-cloud seeding case study using a parcel–DNS (direct numerical simulation) approach, *Atmospheric Chemistry and Physics*, 20(17), pp.10111-10124. https://doi.org/10.5194/acp-20-10111-2020, 2020.

892   Chushak, Y.G. and Bartell, L.S.: Simulations of spontaneous phase transitions in large, deeply supercooled clusters
893   of SeF6, The Journal of Physical Chemistry B, 103(50), pp.11196-11204, https://doi.org/10.1021/jp992818g,
894   1999.

895   Chushak, Y. and Bartell, L.S.: Crystal nucleation and growth in large clusters of SeF6 from molecular dynamics
896   simulations, The Journal of Physical Chemistry A, 104(41), pp.9328-9336,
897   https://doi.org/10.1021/jp002107e, 2000.

898   COMSOL 2023a Cylindrical System Documentation, Last Accessed Sept 15, 2023
899   https://doc.comsol.com/5.5/doc/com.comsol.help.comsol/comsol_ref_definitions.12.090.html

900   COMSOL 2023b Infinite Element Domain Documentation, Last Accessed Sept 15, 2023
901   https://doc.comsol.com/5.5/doc/com.comsol.help.comsol/comsol_ref_definitions.12.116.html

902   COMSOL 2023c Free Triangular Documentation, Last Accessed Sept 15, 2023
903   https://doc.comsol.com/5.5/doc/com.comsol.help.comsol/comsol_ref_mesh.15.38.html

904   COMSOL 2023d Mapped Documentation, Last Accessed Sept 15, 2023
905   https://doc.comsol.com/5.6/doc/com.comsol.help.comsol/comsol_ref_mesh.20.40.html

906   Cooper, W.A.: Ice initiation in natural clouds. In Precipitation enhancement—A scientific challenge (pp. 29-32).
907   American Meteorological Society, Boston, MA, https://doi.org/10.1175/0065-9401-21.43.29, 1986.

908   DeMott, P.J., Rogers, D.C., Kreidenweis, S.M., Chen, Y., Twohy, C.H., Baumgardner, D., Heymsfield, A.J. and Chan,
909   K.R.: The role of heterogeneous freezing nucleation in upper tropospheric clouds: Inferences from
910   SUCCESS, Geophysical Research Letters, 25(9), pp.1387-1390, https://doi.org/10.1029/97GL03779, 1998.

911   DeMott, P.J., Prenni, A.J., Liu, X., Kreidenweis, S.M., Petters, M.D., Twohy, C.H., Richardson, M.S., Eidhammer,
912   T. and Rogers, D.: Predicting global atmospheric ice nuclei distributions and their impacts on
913   climate, Proceedings of the National Academy of Sciences, 107(25), pp.11217-11222,
914   https://doi.org/10.1073/pnas.0910818107, 2010.

915   Djikaev, Y.S., Tabazadeh, A., Hamill, P. and Reiss, H.: Thermodynamic conditions for the surface-stimulated
916   crystallization of atmospheric droplets, The Journal of Physical Chemistry A, 106(43), pp.10247-10253,
917   https://doi.org/10.1021/jp021044s, 2002.

918   Djikaev, Y.S. and Ruckenstein, E.: Thermodynamics of heterogeneous crystal nucleation in contact and immersion
919   modes, The Journal of Physical Chemistry A, 112(46), pp.11677-11687, https://doi.org/10.1021/jp803155f,
920   2008.

921   Fletcher, N.H.: The physics of rainclouds/NH Fletcher; with an introductory chapter by P. Squires and a foreword by
922   EG Bowen. Cambridge University Press, https://doi.org/10.1002/qj.49708837821, 1962.

923   Fukuta, N.: Theories of competitive cloud droplet growth and their application to cloud physics studies, Journal of
924   the Atmospheric Sciences, 49, 1107–1114, https://doi.org/10.1175/1520-
925   0469(1992)049<1107:TOCCDG>2.0.CO;2., 1992.

926   Grabowski, W.W. and Wang, L.P.: Growth of cloud droplets in a turbulent environment, Annual Review of Fluid
927   Mechanics, 45, pp.293-324, https://doi.org/10.1146/annurev-fluid-011212-140750, 2013.

928   Hall, W.D. and Pruppacher, H.R.: The survival of ice particles falling from cirrus clouds in subsaturated air, *Journal*
929   *of   Atmospheric   Sciences,*   33(10),   pp.1995-2006,   https://doi.org/10.1175/1520-
930   0469(1976)033<1995:TSOIPF>2.0.CO;2, 1976.

931   Jakobsson, J.K., Waman, D.B., Phillips, V.T. and Bjerring Kristensen, T.: Time dependence of heterogeneous ice
932   nucleation by ambient aerosols: laboratory observations and a formulation for models. *Atmospheric*
933   *Chemistry and Physics*, *22*(10), pp.6717-6748, https://doi.org/10.5194/acp-22-6717-2022, 2022.

934   Kanji, Z. A., Ladino, L. A., Wex H., Boose, Y., Burkert-Kohn, M., Cziczo, D. J. and Krämer, M.: Overview of Ice
935   Nucleating Particles, *Meteor. Monogr.*, **58**, 1.1–1.33, https://doi.org/10.1175/AMSMONOGRAPHS-D-16-
936   0006.1, 2017.

937   Khain, A.P. and Pinsky, M.: Physical processes in clouds and cloud modeling, Cambridge University Press, 2018.

938   Khvorostyanov, V.I. and Curry, J.A.: A new theory of heterogeneous ice nucleation for application in cloud and
939   climate   models,   *Geophysical   Research   Letters,*   27(24),   pp.4081-4084,
940   https://doi.org/10.1029/1999GL011211, 2000.

941   Khvorostyanov, V. and Sassen, K.: Toward the theory of homogeneous nucleation and its parameterization for cloud
942   models, *Geophysical research letters*, 25(16), pp.3155-3158, https://doi.org/10.1029/98GL02332, 1998.

943   Kinzer, G. D., and Gunn, R.: The evaporation, temperature and thermal relaxation-time of freely falling waterdrops,
944   *J. Meteor.,* 8, 71–83. https://doi.org/10.1175/1520-0469(1951)008<0071:TETATR>2.0.CO;2, 1951.

945   Lü, Y.J., Xie, W.J. and Wei, B.: Observation of ice nucleation in acoustically levitated water drops, Applied Physics
946   Letters, 87(18), http://dx.doi.org/10.1063/1.2126801, 2005.

947   Marquis, J. and Harrington, J.Y.: Radiative influences on drop and cloud condensation nuclei equilibrium in
948   stratocumulus, *Journal   of   Geophysical   Research: Atmospheres,* 110(D10),
949   https://doi.org/10.1029/2004JD005401, 2005.

950   Mason, B. J.,: The Physics of Clouds, Clarendon Press, Oxford, 671pp.1971.

951   Maxwell, J.C.: Theory of the wet bulb thermometer, Scientific Papers of James Clerk Maxwell, 2, p.636, 1890.

952   Meyers, M.P., DeMott, P.J. and Cotton, W.R.: New primary ice-nucleation parameterizations in an explicit cloud
953   model, *Journal of Applied Meteorology and Climatology,* 31(7), pp.708-721, https://doi.org/10.1175/1520-
954   0450(1992)031<0708:NPINPI>2.0.CO;2, 1992.

955   Mossop, S.C., Ruskin, R.E. and Heffernan, K.J.: Glaciation of a Cumulus at Approximately− 4C, *Journal of*
956   *Atmospheric   Sciences,*   25(5),   pp.889-899,   https://doi.org/10.1175/1520-
957   0469(1968)025<0889:GOACAA>2.0.CO;2, 1968.

958   Murray, B.J., O'sullivan, D., Atkinson, J.D. and Webb, M.E.: Ice nucleation by particles immersed in supercooled
959   cloud droplets, Chemical Society Reviews, 41(19), pp.6519-6554, doi:10.1039/c2cs35200a., 2012.

960   Phillips, V.T., DeMott, P.J. and Andronache, C.: An empirical parameterization of heterogeneous ice nucleation for
961   multiple chemical species of aerosol, *Journal of the Atmospheric Sciences,* 65(9), pp.2757-2783,
962   https://doi.org/10.1175/2007JAS2546.1, 2008.

963 Plummer, D.M., McFarquhar, G.M., Rauber, R.M., Jewett, B.F. and Leon, D.C.: Structure and statistical analysis of
964   the microphysical properties of generating cells in the comma head region of continental winter cyclones,
965   *Journal of the Atmospheric Sciences,* 71(11), pp.4181-4203, https://doi.org/10.1175/JAS-D-14-0100.1, 2014.

966 Plummer, D. M., G. M. McFarquhar, R. M. Rauber, B. F. Jewett, and Leon., D. C.: Microphysical properties of
967   convectively generated fall streaks in the comma head region of continental winter cyclones, *J. Atmos.*
968   *Sci.*, **72**, 2465–2483, doi:10.1175/JAS-D-14-0354.1, 2015.

969 Pruppacher, H. R., and Klett, J. D.: *Microphysics of Clouds and Precipitation.* 2d ed. Kluwer Academic, 954 pp.,
970   1997.

971 Ramelli, F., Henneberger, J., David, R.O., Bühl, J., Radenz, M., Seifert, P., Wieder, J., Lauber, A., Pasquier, J.T.,
972   Engelmann, R. and Mignani, C.: Microphysical investigation of the seeder and feeder region of an Alpine
973   mixed-phase cloud, Atmospheric Chemistry and Physics, 21(9), pp.6681-6706, https://doi.org/10.5194/acp-
974   21-6681-2021, 2021.

975 Rauber, R. M., Grant, L. O.: The characteristics and distribution of cloud water over the mountains of northern
976   Colorado during winter-time storms. Part II: Spatial distribution and microphysical characteristics. J.
977   Climate Appl. Meteor., 25, 489–504, https://doi.org/10.1175/1520-
978   0450(1986)025<0489:TCADOC>2.0.CO;2, 1986.

979 Roach, W. T.: On the effect of radiative exchange on the growth by condensation of a cloud or fog droplet, *Quart. J.*
980   *Roy. Meteor. Soc.,* 102, 361–372, https://doi.org/10.1002/qj.49710243207, 1976.

981 Rogers, R.R. and Yau, M.K.: *A Short Course in Cloud Physics*. Pergamon Press, 294 pp., 1989.

982 Rowe, P.M., Fergoda, M. and Neshyba, S.: Temperature-dependent optical properties of liquid water from 240 to 298
983   K. *Journal of Geophysical Research: Atmospheres*, 125(17), https://doi.org/10.1029/2020JD032624, 2020.

984 Roy, P., Rauber, R.M. and Girolamo, L.D.: A closer look at the evolution of supercooled cloud droplet temperature
985   and lifetime in different environmental conditions with implications for ice nucleation in the evaporating
986   regions of clouds, *Journal of the Atmospheric Sciences*. https://doi.org/10.1175/JAS-D-22-0239.1, 2023.

987 Satoh, I., Fushinobu, K. and Hashimoto, Y.: Freezing of a water droplet due to evaporation—heat transfer dominating
988   the evaporation–freezing phenomena and the effect of boiling on freezing characteristics, *International*
989   *Journal of Refrigeration*, 25(2), pp.226-234, http://dx.doi.org/10.1016/S0140-7007(01)00083-4, 2002.

990 Scardovelli, R. and Zaleski, S.: Direct numerical simulation of free-surface and interfacial flow, *Annual review of fluid*
991   *mechanics*, *31*(1), pp.567-603. https://doi.org/10.1146/annurev.fluid.31.1.567, 1999.

992 Sedunov, Y. S.: *Physics of the Drop Formation in the Atmosphere*, John Wiley and Sons, 234 pp., 1974.

993 Shaw, R.A., Durant, A.J. and Mi, Y.: Heterogeneous surface crystallization observed in undercooled water, *The*
994   *Journal of Physical Chemistry B*, 109(20), pp.9865-9868, https://doi.org/10.1021/jp0506336, 2005.

995 Srivastava, R.C. and Coen, J.L.: New explicit equations for the accurate calculation of the growth and evaporation of
996   hydrometeors by the diffusion of water vapor, *Journal of Atmospheric Sciences,* 49(17), pp.1643-1651,
997   https://doi.org/10.1175/1520-0469(1992)049<1643:NEEFTA>2.0.CO;2, 1992.

998 Standard Atmosphere: ISO 2533:1975, updated 2021: https://www.iso.org/standard/7472.html, 2021, last accessed
999   09/26/2022.

Szakáll, M., Debertshäuser, M., Lackner, C.P., Mayer, A., Eppers, O., Diehl, K., Theis, A., Mitra, S.K. and Borrmann, S.: Comparative study on immersion freezing utilizing single-droplet levitation methods, Atmospheric Chemistry and Physics, 21(5), pp.3289-3316, https://doi.org/10.5194/acp-21-3289-2021, 2021.

Tabazadeh, A., Djikaev, Y.S., Hamill, P. and Reiss, H.: Laboratory evidence for surface nucleation of solid polar stratospheric cloud particles, *The Journal of Physical Chemistry A*, 106(43), pp.10238-10246, https://doi.org/10.1021/jp021045k, 2002a.

Tabazadeh, A., Djikaev, Y.S. and Reiss, H.: Surface crystallization of supercooled water in clouds, *Proceedings of the National Academy of Sciences*, 99(25), pp.15873-15878, https://doi.org/10.1073/pnas.252640699, 2002b.

Tessendorf, S.A., Boe, B., Geerts, B., Manton, M.J., Parkinson, S. and Rasmussen, R.: The future of winter orographic cloud seeding: A view from scientists and stakeholders, Bulletin of the American Meteorological Society, 96(12), pp.2195-2198, https://doi.org/10.1175/BAMS-D-15-00146.1, 2015.

Tessendorf, S., Ikeda, K., Rasmussen, R., French, J., Rauber, R., Korolev, A., Xue, L., Blestrud, D., Dawson, N., Meadows, M., Kunkel, M. and Parkinson, S.: Characteristics of Generating Cells in Wintertime Orographic Clouds. Journal of the Atmospheric Sciences, 81(3), pp. 649-673. https://journals.ametsoc.org/view/journals/atsc/81/3/JAS-D-23-0029.1.xml, 2024.

Vaillancourt, P.A., Yau, M.K. and Grabowski, W.W.: Microscopic approach to cloud droplet growth by condensation. Part I: Model description and results without turbulence, *Journal of the Atmospheric Sciences*, 58(14), pp.1945-1964, https://doi.org/10.1175/1520-0469(2001)058%3C1945:MATCDG%3E2.0.CO;2, 2001.

Vali, G.: Freezing Rate Due to Heterogeneous Nucleation. *J. Atmos. Sci.*, **51**, 1843–1856, https://doi.org/10.1175/1520-0469(1994)051<1843:FRDTHN>2.0.CO;2, 1994.

Volmer, M.: Kinetic der Phasenbildung (Steinkopff, Dresden, Leipzig), 1939.

Wang, Y., McFarquhar, G.M., Rauber, R.M., Zhao, C., Wu, W., Finlon, J.A., Stechman, D.M., Stith, J., Jensen, J.B., Schnaiter, M. and Järvinen, E.: Microphysical properties of generating cells over the Southern Ocean: Results from SOCRATES, *Journal of Geophysical Research: Atmospheres*, 125(13), https://doi.org/10.1029/2019JD032237, 2020.

Watts, R.G.: Relaxation time and steady evaporation rate of freely falling raindrops, *Journal of Atmospheric Sciences,* 28(2), pp.219-225, https://doi.org/10.1175/1520-0469(1971)028<0219:RTASER>2.0.CO;2, 1971.

Watts, R.G. and Farhi, I.: Relaxation times for stationary evaporating liquid droplets, *Journal of the Atmospheric Sciences,* 32(9), pp.1864-1867, https://doi.org/10.1175/1520-0469(1975)032%3C1864:RTFSEL%3E2.0.CO;2, 1975.

Welti, A., Lüönd, F., Kanji, Z.A., Stetzer, O. and Lohmann, U.: Time dependence of immersion freezing: an experimental study on size selected kaolinite particles. *Atmospheric Chemistry and Physics*, 12(20), pp.9893-9907, 2012.

Wexler, A.: Vapor pressure formulation for water in range 0 to 1008C. A revision, *J. Res. Natl. Bur. Stand.* (U.S.), 80A, 775–785, https://doi.org/10.6028%2Fjres.080A.071, 1976.

White, F.M.: Viscous Fluid Flow, 3rd ed., McGraw-Hill, 2006, 656 pp.

1036 Wright, T. P., and Petters, M.D.: The role of time in heterogeneous freezing nucleation, *J. Geophys. Res.*, 118, 3731–
1037   3743, https://doi.org/10.1002/jgrd.50365, 2013.

1038 Yang, K., Hong, F. and Cheng, P.: A fully coupled numerical simulation of sessile droplet evaporation using Arbitrary
1039   Lagrangian–Eulerian formulation. *International Journal of Heat and Mass Transfer*, *70*, pp.409-420,
1040   https://doi.org/10.1016/j.ijheatmasstransfer.2013.11.017, 2014.

1041 Young, K. C.: The Role of Contact Nucleation in Ice Phase Initiation in Clouds, *Journal of the Atmospheric Sciences,*
1042   31, 768–776,
1043   https://doi.org/10.1175/1520-0469(1974)031<0768:TROCNI>2.0.CO;2, 1974.

1044 Zaremba, T.J., Rauber, R.M., Heimes, K., Yorks, J.E., Finlon, J.A., Nicholls, S.D., Selmer, P., McMurdie, L.A. and
1045   McFarquhar, G.M.: Cloud-Top Phase Characterization of Extratropical Cyclones over the Northeast and
1046   Midwest United States: Results from IMPACTS, Journal of the Atmospheric Sciences, 81(2), pp.341-361,
1047   https://doi.org/10.1175/JAMC-D-22-0154.1, 2024.